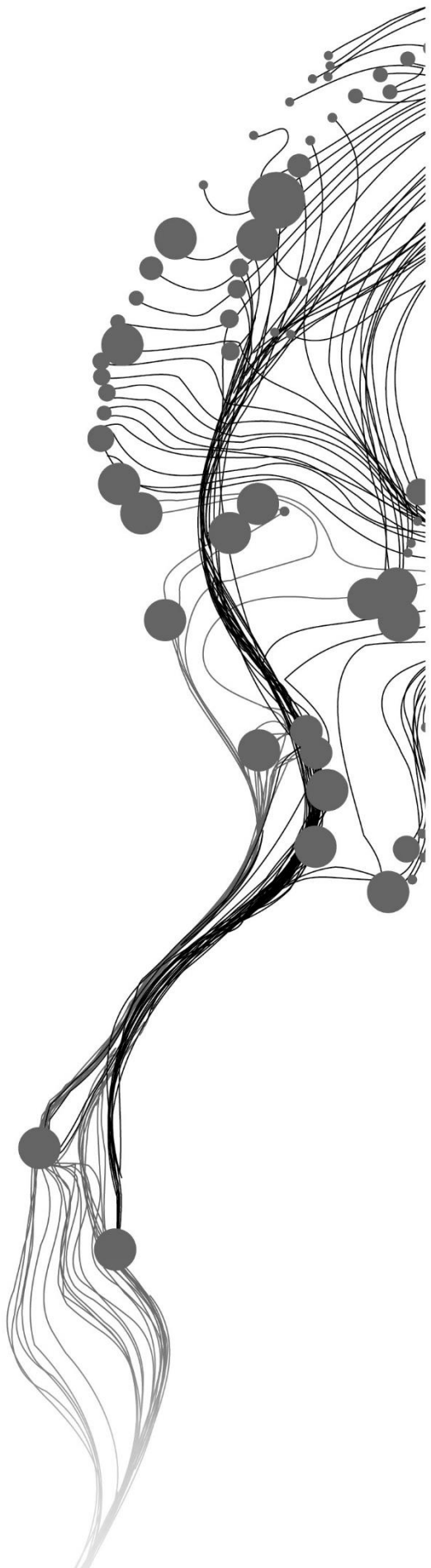# EVALUATION OF TEXTURES ASSOCIATED WITH CARLIN-TYPE GOLD DEPOSIT USING HYPERSPECTRAL IMAGING

OROGHENE OLUWADARA CHOKOR
May, 2019

SUPERVISORS:

Dr. F.J.A. van Ruitenbeek
Dr, H.M.A. van der Werff

EVALUATION OF TEXTURES ASSOCIATED WITH CARLIN-TYPE GOLD DEPOSIT USING HYPERSPECTRAL IMAGING

OROGHENE OLUWADARA CHOKOR
Enschede, The Netherlands, May 2019

Thesis submitted to the Faculty of Geo-Information Science and Earth Observation of the University of Twente in partial fulfilment of the requirements for the degree of Master of Science in Geo-information Science and Earth Observation.
Specialization: Applied Earth Sciences

SUPERVISORS:
Dr. F.J.A. van Ruitenbeek
Dr. H.M.A. van der Werff

THESIS ASSESSMENT BOARD:
Prof. Dr. F.D. van der Meer (Chair)
Prof. Dr. Kim Hein (External Examiner, University of Witwatersrand)

ABSTRACT

This research aimed to map textures of carlin-type gold deposits using hyperspectral shortwave infra-red images and RGB photo images which may be indicative of gold mineralization with the study area. The samples used in this study were acquired by Barrick Gold Corporation. The drill cores were accompanied by auxiliary data – fire assay – showing the concentration of gold and arsenic; X-ray diffraction Data (XRD), showing the minerals in some samples from the study area and Red Green Blue band (RGB) photos of the samples.

The samples were inspected, and their textures were identified. Then images of the samples were acquired using a hyperspectral sensor. The hyperspectral shortwave infrared images were pre-processed and processed to create wavelength maps and band ratios. Wavelength maps are image products whose bands contain images representing the wavelength positions and depth of the first, second absorption feature and third absorption feature contained in the SWIR images. The SWIR and RGB images were classified using a decision tree which relies on given threshold values and Boolean operators to subset the image data until certain criterions were achieved. The image products were used in the decision tree classification to map the hyperspectral images based on the position and depth of its mineralogical constituent which had been highlighted by the wavelength maps. While the RGB images were classified based on the colour ratio of the RGB bands. Then, a portable X-ray fluorescence device was used to measure the concentration of the constituent elements, particularly gold, present in drill core samples. The two minerals of interest were gold and arsenic. Measurement was carried out on identified textures such as the different matrix of the drill cores as well as veins and clast.

The mineral maps from the two images performed well in highlighting textures from the samples. Textures such as veins, clasts and breccias, homogenous and layered matrixes were identified. It was observed from the SWIR image products that the Porphyry samples had been altered. They contained white micas at shallow depths and were gradually altered with increasing depth into kaolinite. The calcerous silttone samples had also been altered. The minerals had either been completely replaced by whit micas or the carbonate had been mixed with white micas. The fire assay, as well as the XRF measurements, show that that white mica and montmorillonite veins in dark grey silty non- carbonate matrix contained high gold concentrations above 11ppm, phengite vein also contained high gold concentration while calcite veins in the same type of matrix contained little to no gold. Also, silty grey matrix with carbonates show indication of Gold but had values that were below the reliable detection limit of the XRF. The RGB images could identify these veins but could not differentiate between calcite veins, which were mostly indicative of the absence of gold; from white micas and clay veins which contained gold, sometimes in high proportions. Also fined grained carbonate matrixes show indication of gold but their measurements were below the detection limit of the XRF and require further investigations because they may or may not actually contain gold.

ACKNOWLEDGEMENTS

TABLE OF CONTENTS

LIST OF FIGURES

LIST OF TABLES

1. INTRODUCTION

1.1. Background

Mineral prospecting of gold traditionally dealt with gold deposits that were contained in quartz veins of crystalline rocks, whether of igneous or metamorphic origin, until the later part of the 1900's when sedimentary hosted deposits became of economic importance. The first Carlin-type gold deposit was discovered in 1960 near the town of Carlin, Nevada and subsequently, similar deposits were found along the NW and NE trending shear zones called the carlin trend (Li & Peters, 1998). While epithermal gold deposits are formed from gold saturated hydrothermal fluids, carlin type gold are formed for fluids that are undersaturated with Au. The key to the formation of large scale carlin type deposits is the ability for Arsenic pyrite to absorb the solid state gold form these undersaturated fluids. (Zhu, An, & Tan, 2011).

Ore texture plays a role in the identification of nature and the forming process of an ore. It can be defined as the spatial relationship between mineral grain and reveals information about the mineralogy, the origin and the geologic setting of their mineralization. Therefore, a proper understanding of these textures helps to understand the history of an ore (Barton, 1991; Craig & Vaughan, 2005). Some textures are associated with metamorphism, while others are indicative of hydrothermal alteration processes.

The deposition of ore minerals during the formation of hydrothermal ore deposits is often related to specific hydrothermal alteration zones. Identification of mineralogy and textures related to alteration offer the possibility of characterising an ore and is particularly important because they are associated with deposits rich in metallic ores of high economic grade (Dalm, 2018; Govil, 2015).

The study of patterns and textures of rocks have been observed and recorded since before the 19th century. Historically, ore textures are investigated using petrography and ore microscopy. Samples were primarily analysed under reflected and transmitted light. Interpretation involved applying geologic principles on the microscopic scale (Barton, 1991) to analysis grain-size, relationship, grain boundary shape and orientation fabric (Higgins, 2006).

Laboratory-based investigation of earth materials using hyperspectral images has been successfully carried out (Homayouni & Roux, 2014). Advances in hyperspectral sensors have provided researchers with the opportunity to study rocks at a higher spatial dimension. The higher resolution hyperspectral images have allowed discrimination of mineral spectra in finely grained lithologies like carbonate rocks (Bevan, 2018). These images incorporate both high spectral and spatial information of the imaged rock samples and can now reveal information that could only be previously assessed using thin section petrography and microscopy (Turner et al., 2017). This allows the spectroscopic analysis of rocks carried out in the laboratory to provide high levels of textural and mineralogical information (Turner et al., 2017). The result of the analysis of a hyperspectral image is the proper classification every pixel in the image of the observed material based on each pixel's unique spectral curve (Kamruzzaman & Sun, 2016).

Earth materials like rocks are investigated and identified based on their spectra absorption features at specific wavelengths of the electromagnetic spectrum. This is possible because of the high spectral resolution of a hyperspectral sensor that acquires images where every pixel of the image contains a spectrum that is made up of data points representing a large number of consecutive wavelengths the sensor images a given material (Kamruzzaman & Sun, 2016; Turner et al., 2017). The spectral absorption

features of materials are influenced by different electronic or vibrational processes of their molecules and are diagnostic for a given material (Scott & Yang, 1997; Swayze et al., 2014; van der Meer, 2018). And in geology, they allow for the proper identification of the mineralogy of rocks and earth materials. Knowledge of the mineralogy of rock can aid in understanding the geological processes of their formation, deformation and or alteration. (Asadzadeh & de Souza Filho, 2016). For mineral exploration, mapping the spatial distribution of spectrally active minerals in the 0.4 to a 2.5µm range of the electromagnetic spectrum has proven effective in evaluating patterns formed during the hydrothermal alteration process (Swayze et al., 2014). The aluminium hydroxyl ion (Al-OH) of phyllosilicates minerals like clays and white micas exhibits as an absorption feature between 2100nm and 2250nm wavelength while the carbonate ion CO_3^{2-} present in carbonate minerals exhibits absorption features at 2300nm to 2400nm wavelength range (Swayze et al., 2014; van der Meer, 2004).

Two useful methods used in mineral identification and mapping include band ratios and mapping the wavelength position of the deepest absorption features of images. Van Ruitenbeek et al., 2014 developed the method of mapping the wavelength position of the deepest absorption feature between 2.1-2.4µm to create surface mineralogical maps. The method helps to highlight spectral differences of minerals that have different absorption features at different wavelength within a hyperspectral image. Band ratios are also useful in differentiating between minerals with absorption feature near the same wavelength position. The ratios can highlight subtle shifts in spectral features (Van Ruitenbeek et al., 2006). This is applicable to delineating between clays and white micas groups which share similar absorption feature in the 2.1-2.4µm range.

Several types of research have been done on investigating rock textures, characterising ore deposits based on their mineralogy and textures, developing models to sort ores from gangue and improving the parameters of these models (Gay, 2004; Hilden & Powell, 2017; Iyakwari et al., 2017; Pérez-barnuevo et al., 2018).

Goetz et al. (2009) researched on copper ores to measure gangue concentrations employed near-infrared spectroscopy supplemented by XRD analysis to develop a model used to predict the concentrations of quantifying swelling clays. Research analysis of porphyry Copper ore carried out by Dalm et al., (2014) mapped minerals spectrally active in the near infrared range. It established an indirect relationship between copper ore grade and near-infrared active minerals. While the test-work did not directly identify spectral features that related to the Copper ore grade, it was able to correlate minerals such as high crystalline white mica with high copper ore grade identified from geochemical analysis.

Bevan (2018) employed high-resolution short-wave infrared (SWIR) images to characterise the alteration of the Cortez hill deposit. Part of his research involved mapping the spatial distribution of hydrothermal alteration minerals and a qualitative investigation of textures associated with gold mineralisation. Hilden & Powell (2017) developed a model for simulating multi-mineral rock textures to predict liberation characteristics using parameters describing grain and grain size distribution. They fitted the parameters of their model by measuring corresponding mineral liberation data. Guiral-Vega (2018) carried out research to characterise the textures and mineralogy of two spodumene pegmatite deposits within the Kaustinen Li province, Finland. Drill cores from the deposits were logged and classified into twelve textural classes representing the ore and host rock. The mineral phases within each textural class were determined using representable image patches for each mineral phase, image segmentation analysis and machine learning random forest model was used to estimate the spodumene yield. Pérez-barnuevo et al. (2018) assessed the potential of drill core textures as geo-metallurgical indicators of iron ore in Quebec. The methodology involved investigating the liberation process of the ore and characterising the mineralogy and grain size distribution of identified textural patterns.

1.2. Previous Work

Some researchers have already been carried out analyses on the Cortez hill deposit using hyperspectral imagery. Two researchers who have some samples used in this research include Bevan (2018) and Dalm (2018). Bevan (2018) researched the usability of high-resolution shortwave infrared hyperspectral images to characterize the hydrothermal alteration at Cortez hill. He mapped the hydrothermal alteration minerals of 19 drill cores to highlight variations in mineral type and their composition variations. His maps also highlighted porphyritic-porphyroblastic mineral textures in gold hosting rocks of Cortez hill. The minerals he identified included carbonate minerals, white micas, clay minerals, tremolite and talc, chlorite and mixed mineral classes and these were validated using optical petrography. This allowed the identification of the alteration type that had taken place in the study area, expressed by the replacement of chlorite talc and tremolite by white mica minerals.

Dalm (2018) researched to explore the benefits of using sensors for real-time raw material characterization in mining and sorting of the hydrothermal ore deposit. He proposed that with increasing demand for mineral resources, sensor-based sorting machines could be incorporated into mineral processing to improve sorting. He noted that because most ores are polymineralic rocks with the important economic minerals occur in small proportions grain sizes, there are no known sensors that can be used to detect the grade of ore particles.

For his work; he used samples from three different types of ore deposits, the Los Bronces porphyry copper deposits, the Lagunas Norte epithermal gold-silver deposit and the Cortez hill Carlin-type gold deposits. From visible near-infrared (VNIR) and shortwave infrared (SWIR) images of his samples, he extracted spectral features such as absorption location and depth of the most dominant mineral, mica crystallinity which is the ratio of the depth of Al-OH absorption at 2200nm and depth water (H_2O) absorption at 1900nm and ferrous ion absorption between 1450 and 1850nm. These were used together with XRF measurements/and or fire assay data in multivariate regression, partial least square regression (PLSR) and discriminant analysis (PLS-DA) to identify variables that contain information useful to create a model for the classification of spectral data.

For Cortez hill, he used 629 drill core samples in the PLS-DA model to identified minerals characteristics of samples with a gold grade less than 0.15ppm which was classified as waste and greater than 5.14ppm, carbon content and sulphur content was used to predicts a response for each measured spectrum. He observed that calcite was an indicator of waste while dolomite was associated with ore samples. He also observed that white mica samples with absorption feature lower than 2205nm were ore samples (> 0.15ppm) with 17% having an average of 21.3ppm while those occurring between 2205 and 2210nm were waste (<0.15ppm).

1.3. Problem Statement

The exploration of mineral deposits by mapping the distribution of associated minerals has its limitations. It is essential to incorporate textural information during the investigation because they provide the opportunity to better understand the mineralisation processes of an ore body further. Ore deposits have been investigated by using short wave infrared to mapping alteration minerals common to the deposit. However, it is important to combine textural information with this mineralogical information to better characterize a deposit. By evaluating the relationship between identified textures, their mineralogy and the concentration of gold within samples, a better understanding of the ore deposit will be obtained. At the end, textures that are indicative of the ore mineralization will be determined and the impact of possible variations to these textures across the drill hole may be understood.

1.4. Objectives and Research Question

1.4.1. Aim

This project aims to evaluate the relationship between indicator textures and gold ore grades; by analysing and measuring texture parameters and their variation with depth using high-resolution RGB and short wave infrared hyperspectral images and comparing with XRF data of drill core samples from Cortez Hills.

1.4.2. Objectives

The specific objectives include:
- visual inspection and qualitative interpretation of drill cores to create texture inventory,
- mineral mapping using decision tree classification of SWIR hyperspectral images and supervised classification of RGB images to highlight textures,
- determination of the distribution of gold and arsenic in the drill cores,
- evaluating the relationship between minerals, textures and gold concentration.

1.4.3. Research questions
- What type of lithologies is present?
- Are there variations in textures within the same lithologies?
- What minerals and textures are identified in the short-wave infrared range hyperspectral images?
- What comparisons can be made between texture measured in the two RGB and SWIR images?
- Are there textures better observed in the RGB or in SWIR? What sort of textures are they?
- Do textures change with depths? What are the causes of these changes?
- What are the effects of weathering on these textures?
- What sort of relationship, exists between the different textures and the gold concentrations of the ore?

1.5. Hypothesis

Specific textures like veins and breccias can be indicative of gold mineralization.

1.6.   Study Area

The study area is in Cortez Hills, located at the geographic coordinates 40°10'11"N, 116°36'31"W, in Eureka County, north-central Nevada, USA. The study area is located within the Carlin-trend (*see Figure 1*) and is a part of the Battle Mountain-Eureka trend. It is one of the three most prolific gold belts in the world (Garwin, 2005). The belt is approximately 60 km by 7 km and is trending north-west.

1.6.1.   Geological Setting

The gold deposits are hosted in carbonate and siliciclastic rocks of lower Paleozoic in the lower plate of the Robert Mountain thrust (Colgan et al., 2008; Garwin, 2005; Gilluly & Masursky, 1965). Lithologies in the lower plate include the Cambrian Harmburg Dolomite; Ordovician Eureka Quartzite and the Hanson Creek Formation (Gilluly & Masursky, 1965). This sequence is overlain by Ordovician through Devonian siliciclastic sequence of the upper plate of Roberts Mountain allochthon that was emplaced by a Thrust fault in Mississippian time (Hofstra & Cline, 2000). The lithologies in Upper late contains lower and middle Ordovician Vinni and Valmy Formations, Elder sandstone and Slaven. They are made up of argillites, cherts, quartzite, sandstones (Gilluly & Masursky, 1965).

Three episodes of intrusions occur along with the Car0 lin trend; the Mill Canyon Stock, a Jurassic intrusion of Biotite Quartz Monzonite, common in the Carlin trend. Eocene calc-alkaline porphyritic Dacite and Rhyolite dykes are trending north-northwest to the north-northeast and Miocene rhyolitic events. Crosscutting field relationship and Argon radiometric dating indicate the emplacement of these Eocene dykes occur at the same time as the gold mineralisation in the carlin trend (Garwin, 2005).

The hydrothermal alteration also occurred within the trend. It is characterized by decarbonatization and dolomitization of the carbonate host rocks; sulfidation of iron and the silicification of limestone, and argillic alteration of silicates (Garwin, 2005; Hofstra & Cline, 2000). Structures in the rock sequence include a regional anticlinorium and is exposed as anticlinal hinge zones trending northwest that approximately coincides with the central axis of the Carlin Trend and faults and fractures trending north-east and north north-west (Garwin, 2005).

1.6.2.   Ore Deposit

The Carlin-type gold deposit is a sedimentary hosted disseminated gold deposit. The composition, permeability and porosity of its host rocks play a significant role in the mineralisation of gold in the trend (Garwin, 2005). The gold occurs as sub-micron particles in arsenic-pyrite bearing ores. The main ore stage formed during the cooling and neutralisation of ore fluids by the host rocks at temperature conditions of 250-150°C (Hofstra & Cline, 2000). The presence of hydrogen sulfide in the ore fluids suppressed the solubility of iron, causing sulfidation and the precipitation of gold and pyrite from the fluids. The fluids were probably controlled by the less permeable upper plate of the Roberts thrust mountain into the underlying carbonates along with major structures (Hofstra & Cline, 2000).

The Carlin deposits can be highly profitable to exploit, having grades as high as 8 to 52 g/t Au (Garwin, 2005; Hofstra & Cline, 2000). The Gold bearing mineral is Arsenic-pyrite, other ore minerals include cinnabar, copper oxide, iron oxide, pyrite, nickel-arsenic sulfide, while gangue minerals are calcite and quartz (USGS, n.d.).
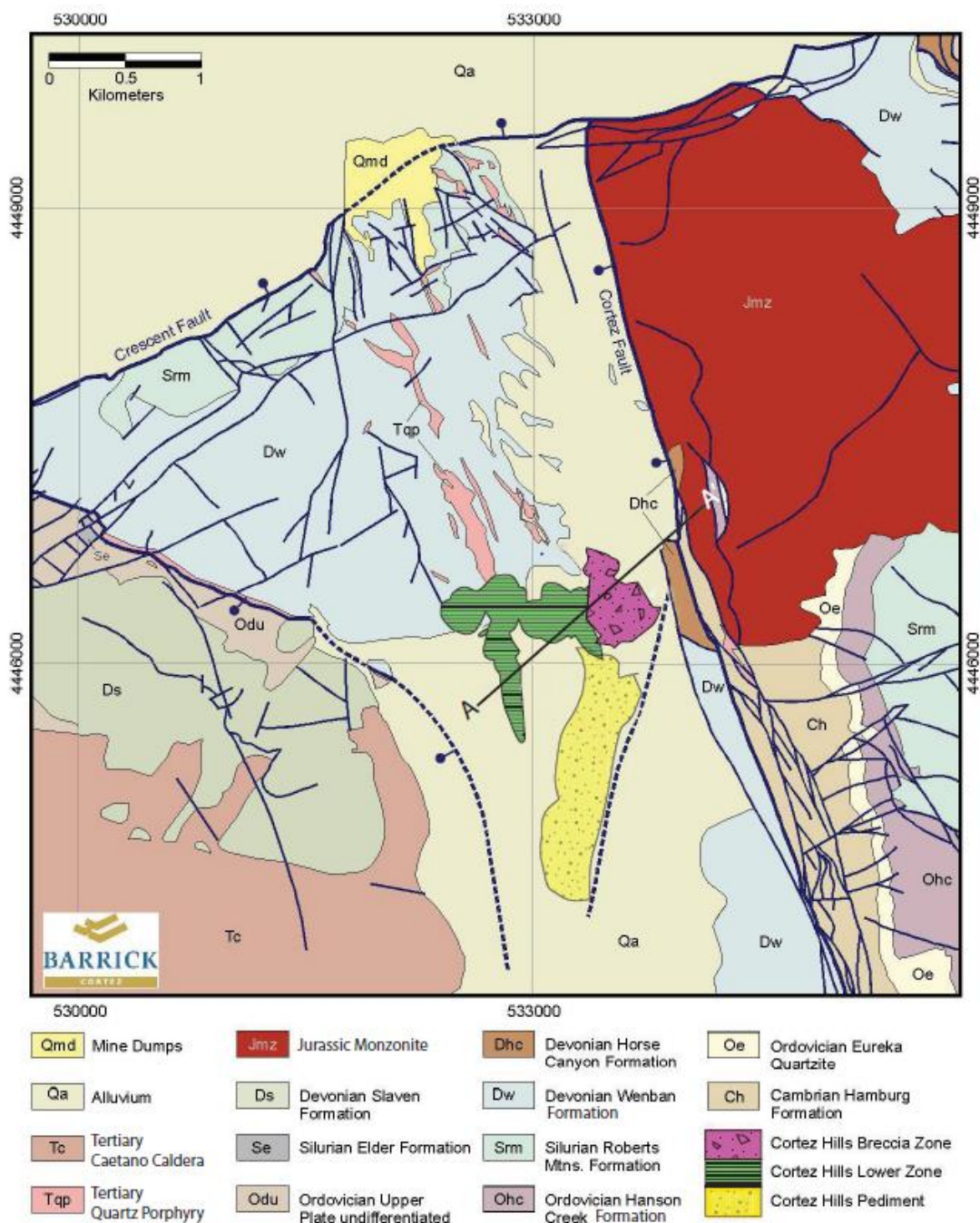
Figure 1: Geological map of Cortez Hills. Source: Clark (2012).

2.   DATA

2.1.   Dataset

The primary datasets used for this research were drill core samples; they came accompanied with auxiliary data containing location, geological information and results of fire assay test.

2.1.1.   Drill cores

The total number of 71 samples obtained from the three boreholes were analysed in this research. These samples were obtained by Barrick Gold Corporation and have Hole ID; CHUE-264, CHUE-279 and CHUE-352. The depth in metres where the samples were obtained from also doubled as their sample. They were approximately 10cm to 20cm in length and 4 to 6cm wide. Some samples were fragmented and smaller than this size. The number off samples and lithologies the samples were obtained from are listed in the table below:

Table 1: Summary of samples used in this research

CHUE 264	No.	CHUE 297	No.	CHUE352	No.
Silty Limestone	14	Silty Micrite	5	Micrite	5
Calcareous Siltstones	5	Calcareous Siltstone	2	Silty Micrite	2
Marble	2	Micrite	4	Calcareous Siltstone	8
Dolomite	1	Dolomite	1	Dolomite	2
Quartz porphyry	3	Quartz Porphyry	12	Quartz Porphyry	4
Feldspar Porphyry	2				
Total	26		24		21

2.1.2.   Auxiliary Borehole Data

The drill cores (see *Figure 2* for example) were accompanied by auxiliary data which were; High-resolution RGB colour photos, geochemical and X-ray powder diffraction (XRD) data. The geochemical analysis data on the drill cores carried out by Barrick Corporation was provided in an excel document with geological and chemical information of the samples at 5 to 10 metres intervals of measurement. The information included the depth the samples were collected (in meters), the formation the samples were obtained from, the type of lithology they were, and their gold concentration obtained through fire assay analysis.

High-resolution RGB photos were also available for this research. These photos were obtained by digital cameras that imaged the samples using 3 bands located at 450nm 550nm and 850nm representing the blue, green and red wavelength range the visible part of the electromagnetic spectrum. The images were acquired in 19-09-2015 by Marinus Dalm and have a spatial resolution of 0.2mm

Dalm (2017) also carried out a XRD analysis to identify the mineralogy of samples obtained from the study area. The XRD analysis is a method used to identify the crystalline structure, physical and chemical properties of a material (Misture & Snyder, 2001). He identified calcite, augite, aluminian, orthoclase, dolomite, tremolite, phlogopite, clinochlore and quartz from samples in the study area. And specifically identified calcite, dolomite, tremolite and quartz from sample E352-1145.

The data was provided in Pdf format and contained information about minerals that have been identified from some of the samples using this method. The identified include

The details of the dataset are summarized in *Table 2* below.

Table 2: showing available dataset used in this research.

Available dataset	Description	Acquired by	Spatial/Spectral Resolution
Drill core samples	74 drill cores with hole ID CHUE-264, CHUE-279 and CHUE-352	Barrick Corporation	
High resolution RGB images	3 band Color photos of samples. Band 1 = 450nm Band 2 =550nm Band 3 = 650nm		0.2mm/ 440, 550, 630nm
XRD	Peak position and intensity of mineral phases.	Marinus Dalm at the Department of Materials Science and Engineering of the Delft University of Technology.	Minerals
Geochemical data (fire assay test)	Excel sheets with: 3-dimension location information, - Lithological Formation and Units, - Fire assay test result showing Au, As, Ag, Cu, Hg, Sb, in ppm while Ca, Mg, S, in percent.	Barrick Corporation. Bureau Veritas Commodities Canada Ltd.	Location: meters, Concentration: parts per million (PPM), and in percents

2.2. Tools and Softwares

The tools and software used in carrying out this research are detailed below.

2.2.1. SisuCHEMA shortwave infrared scanner

The hyperspectral short-wave infrared camera used for this study was the SisuCHEMA Scanner located in the ITC Geoscience laboratory at 0.2mm spatial resolution. This hyperspectral camera has a spectral resolution of 5.6nm and acquires a contiguous spectrum per pixel in the short-wave infrared between 1000 to 2500nm. It employs push-broom imaging technology to scan samples on a moving sample tray and provides high resolution spatial and spectral image (SPECIM, 2015). Its specifications are listed in *Table 3*.

Table 3: Specifications of the hyperspectral camera.

Characteristics	Specifications
Spectral range	1000-2500nm
Spectral sampling/pixel	5.6nm
Spectral resolution FWHM	12nm
Spatial pixels/line	384
Spectral bands	288
Pixel size	0.2- 0.5μm
Illumination	SPECIM's diffuse line illumination unit
Data format	ENVI, MATLAB and R compatible formats

2.2.2. Thermo Scientific Niton XL3t Portable X-Ray Fluorescence sensor

X-ray Fluorescence sensor is a piece of scientific equipment that measures the constituent of a given sample by bombarding the material with X-Rays. This causes the atoms within its molecules to become excited and their electrons to escape to a higher orbit, the electron will eventually lose energy and go back to its original position but during this process, energy is released. This released energy is specific for each mineral. The XRF tool measures this energy and provides an estimate of the minerals within a material. However, for light metals, it provides only an indication unless the material is flushed with Helium.

The device has a limit of detection for each element it investigates. The limit of detection is defined as the "minimum concentration of a substance measured that can be reported with 99% confidence that the analyte concentration is greater than zero and is determined from analysis of a sample in a given matrix containing the analyte" (Environmental Protection Agency, 2016).

According to the documentation of the device, the detection limit of the sensor for gold after 60 seconds/filter of measurement gold is 16ppm while that for Arsenic is 3ppm (Thermo Scientific, 2010). However, increasing the analysis time to 90seconds/filter will reduce the limit by the square root of the addition time (30seconds) while reducing to 15seconds will double this detection limit (Thermo Scientific, 2010).

2.2.3. HypPy3

Hyppy3 is an image classification software developed by (Bakker, 2012). It was used for the conversion of the raw hyperspectral SWIR infrared images into reflectance; for pre-processing the images and for creating wavelength maps and band ratios from them.

2.2.4. ENVI version 5.5

ENVI is a software package developed by Harris Geospatial Solutions, Incorporated for image processing. This software was used to carry out visualization, pixel spectrum inspection and mineral identification, image classification and finally for image masking. Both Decision tree classification and the maximum likelihood classification processes were carried out using this software package.

Figure 2: Displaying samples of drill hole E264 from 51m to 271m.

3.   METHODOLOGY

The methods used in carrying out this research are discussed in this section.

3.1.1.   Sample inspection

This step involved inspecting the samples to identify and understand the physical characteristics of each sample, identify textures contained within the samples and observe the differences between samples from the same lithologies. The first drill hole with Identification number CHUE-264 has 28 samples
The second one, with ID. No. CHUE - 297 has 24 samples while the third drill hole with ID no. CHUE-352 has 21 samples.

3.1.2.   Image acquisition.

The samples were imaged using the SISUCHEMA sensor (see Table 2 for specification). The setup of the sensor used for acquisition is displayed in figure 2a below. The samples were set in a tray filled with beach sand to ensure they were flat and on the same elevation as the sides of the tray (see figure 2b). The tray was set on the sample stage, and before the SWIR images were acquired, the room was darkened to ensure that the only source of light reflecting on the surface of the samples was from the lamps attached to the sensor. All these were done to reduce noise that may be introduced by differences in illumination of the surrounding background.

The acquisition software of the device was set to acquire the images using the following settings of 38.9 frames/sec with a speed of 10mm/s and exposure time of 2.1ms.
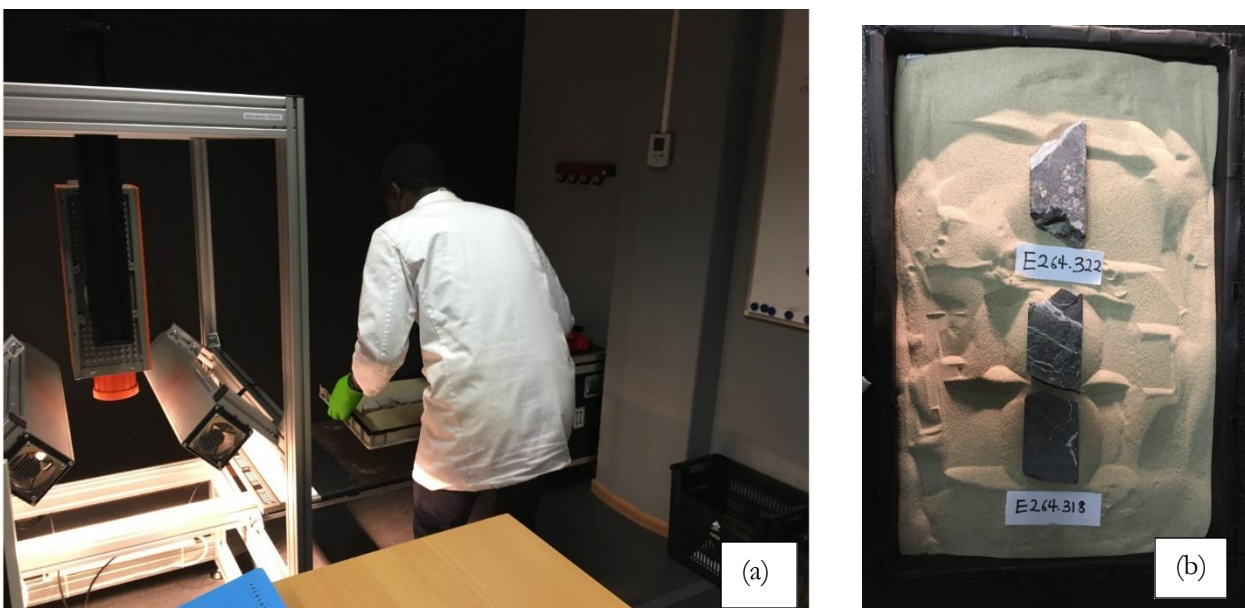
Figure 3: (a)Showing device setup used for image acquisition. (b)Showing samples E264_318m and 322m placed in the sand tray about to be captured using the sisuChema.

3.1.3. Image pre-processing

The hyperspectral images were pre-processed to ensure they were suitable for analysis. These pre-processing steps included conversion to reflection, removal of stripping error during the image acquisition.
The following pre-processing steps were carried out on the images:
- Conversion to reflectance using the dark and white calibration reference of the spectrometer.
- De-striping to remove bad pixels,
- Spectral subset
- Calculation of albedo

The raw hyperspectral acquired was calibrated and converted to reflectance using information obtained from dark and white references. The white reference is obtained from the sensor's white reference surface, which has a near 100% reflectance, and the dark reference was obtained when an image was obtained while the sensor's shutter was closed. This helps correct the instrument noise. The Hyppy software was used to carry out this correction. The next step was to remove bad column strips occurring on every 8th line of the image from the newly calibrated images. This error was corrected by nearest neighbour interpolation using the 'fix 8th SWIR" tool in Hyppy.

The spectral subset was performed in ENVI to remove the first 16 bands from 894nm to 980nm which are noisy and could negatively influence the image processing steps.

The last step carried out in Hyppy was the albedo calculation using Hyppy's log residual tool, which is a tool for normalizing data and removing albedo and atmospheric effects (Bakker, 2012). To achieve this, it calculates the albedo of the image. This albedo image is useful for the classification of dark samples

3.1.4. Image processing

The next step was the image processing steps that were carried out towards creating mineral maps and highlighting textures in the dataset. These steps are further discussed below

3.1.4.1. Wavelength mapping and band ratio

Wavelength mapping was carried out on the hyperspectral images to highlight the wavelength position of the first, second and third deepest absorption for each pixel in the images. The wavelength range of interest in creating the final mineral maps; was range 2100-2400nm because this range contains spectral patterns that are related to OH bonds which are part of the crystalline structure of a mineral and absorption is a sum of the stretching and bending effect of specific bonds in a crystal structure, such as the Al-Oh bonding (Roger N. Clark, 1999). The location of the spectral patterns varies as cation (Aluminium (Al), Silica (Si), Iron (Fe) and Magnesium (Mg)) substitution in the crystal lattice of the mineral changes. This range covers the region where the main diagnostic feature used to delineate between minerals like phyllosilicates, hydroxides, sulphates and carbonates can be found (Clark, 1999; Swayze et al., 2014; van der Meer, 2004). In this research, the two mineral groups of interest were of interest in this research: Minerals with Al-OH bonds (clays) and minerals with CO_3^{2-} (carbonates) because they are useful in identifying hydrothermal alteration minerals (Swayze et al., 2014)

Illite crystallinity band ratio was also created by calculating the ratio of the depth of Al-OH feature at 2200nm and the depth of water absorption feature at 1900nm because of its usefulness in delineating the degree of crystalline and less crystalline clays and white mica. (Dalm, 2018)

3.1.4.2. Mineral identification

The minerals present in some of the samples within the dataset were identified by XRD analysis carried out by Marinus Dalm (2017). He identified Calcite, Augite, Alumina, Orthoclase, Calcite Dolomite, Tremolite, Phlogopite, Clinochlore and Quartz these samples. Bevan (2018) in his research which he carried out on a

subset of the samples used in the study also identified calcite, dolomite, kaolinite, montmorillonite, white micas, tremolite and talc, chlorite and mixtures of carbonates and clays by analysing the spectral features from shortwave-infrared images he acquired analysis and by thin section.

This, together with spectral inspection of pixels highlighted by the wavelength maps and band rations and using the G-Mex Mex (Pontual, S., Merrry, N.,& Gamson, 1997)as a reference, several mineral classes were identified and selected and subsequently used creating and optimizing the decision tree classifier.

3.1.5.   Decision tree classifier

The method chosen for creating mineral maps in this research was the Decision tree classification using the ENVI decision tree module. The Decision Tree classifier is a tree-like algorithm that repetitively divides a dataset into sub-classes (in this case image data) using threshold values and boolean operators until pure data classes are obtained or the classification criteria the user has specified is met (Savan Patel, 2017). This method of classification was used because of the ease of interpretation and the efficiency of its algorithm despite the large data needed to be analysed (Viktor Gavrilov, 2016).

3.1.5.1.   SWIR image classification using decision tree c

The mineral classes identified were used in creating and optimizing the DT classifier for classification of the SWIR image-derived wavelength maps.

The wavelength maps of 2100-2400nm range, the albedo images and the Illite crystallinity band ratios were used as input bands for this DT Classifier. The classifier was optimized iteratively by observing the wavelength maps, the depth maps, spectral of the original pixel after classification until 3 representable DT classifiers capable of classifying all samples were created.

Two DTC were used because while one was capable of the general classification, the other was optimized for dark samples. This was able to discriminate low reflectance grey veins from their surrounding darker pixel using albedo (for example, see *sample 264_502m*) and the last for delineating between White micas in the weathered Porphyries (*see sample e264_271m*). The input bands for used for the DT classifier were; b1 =the band of the wavelength position of the first deepest absorption feature, b2 = the depth of the first absorption feature, b3 = the wavelength position of the second absorption features b4 = depth of the second absorption feature, b7 = illite crystallinity band ratio and b8= albedo band (see Appendix 1 for DT classifiers used for SWIR images).

This step occurred concurrently with the mineral identification step.

3.1.5.2.   RGB image classification using decision tree

The high-resolution RGB images were classified using the decision tree algorithms. The input band for the DT was b1= blue band, b2 = green band and b3 = red band. The RGB images were classified based on the colour of the minerals using 5 classes (see appendix 4 for DT classifier of RGB).

- White/bright minerals,
- Light grey minerals,
- Orange minerals,
- Red minerals,
- Dark grey minerals.

Figure 4: Decision tree classifier for general classification of SWIR images. b1 = wavelength position of deepest absorption feature in 2200-2400nm, b2 = depth of deepest absorption feature, b3 = wavelength position of 2nd deepest absorption feature in 2100-2400nm, b4= depth of 2nd deepest absorption feature; b7= Illite crystallinity index, and b8 = Albedo.

3.1.6. Masking

Masking is a tool used to eliminate unwanted values form a given dataset. In this case, the unwanted values include; slopping edges of the samples, non-flat surfaces/weathered surfaces and the background pixels representing the sand used to prop of the samples to be flat and at the required elevation during image acquisition. After the classification process, these where masked and eliminated. This process was required because the images were then to be further processed using Shaper IDL to extract the textural parameters. Non-flat surfaces and the sand placed in the tray to keep the samples at the required elevation were masked out using the region of interest tool of ENVI.

3.1.7. The acid test for carbonate minerals:

The acid test is a test carried out to determine if a rock contains carbonates or not. Carbonate minerals react to acid and give off carbon dioxide gas (CO_2). This test was carried out on the samples to delineated between mineralized and unmineralized samples of the same lithology.

$$CaCO_3 + 2HNO_3 = H_2O + CO_2 + Ca(NO3)_2 \qquad\qquad ——————— \qquad \textit{Equation 1}$$

3.1.8. Portable XRF Measurement:

The portable XRF sensor was used to measure the concentration of the elements in the samples. Measurement was carried out on the matrix of the samples and on other structures like veins breccias and clasts present in the samples. For most samples, a minimum of 2 repeat measurement was carried out per

location. The device provides a concentration of elements in ppm together with the error margin for each measurement. It should be noted though that according to the documentation of the device, the detection limit for gold after 60 seconds/filter of measurement gold is 16ppm while that for Arsenic is 3ppm (Thermo Scientific, 2010). However, reducing the analysis time to 15seconds will double this detection limit while increasing it to 90seconds/filter will reduce the limit by the square root of the additional time (Thermo Scientific, 2010).

In instances where the explored gold occurs in low concentration or in a concentration below the detection limit of the portable XRF pathfinder elements which can be enriched together with the explored metal are used to locate potential zones of enrichment (Thermo Scientific, 2012). In this research because of the geochemistry of the deposit, as stated by Wilson et al. (1994) " Carlin type deposits are characterized by high concentrations of Au, Ag, As, Sb, Ba, Ti, and Hg Arsenic was selected as the pathfinder mineral. Arsenic (As). Other pathfinder minerals for Carlin type gold include Thallium (Tl), Mercury (Hg), antimony (Sb) and Silver (Ag) because they show high correlation with gold mineralization (Wilson et al., 1994). For this research, measurements below 11ppm, but give actual values instead of returning 'LOD' and having a low error with moderate to high arsenic was considered to be indicative of the presence of gold.
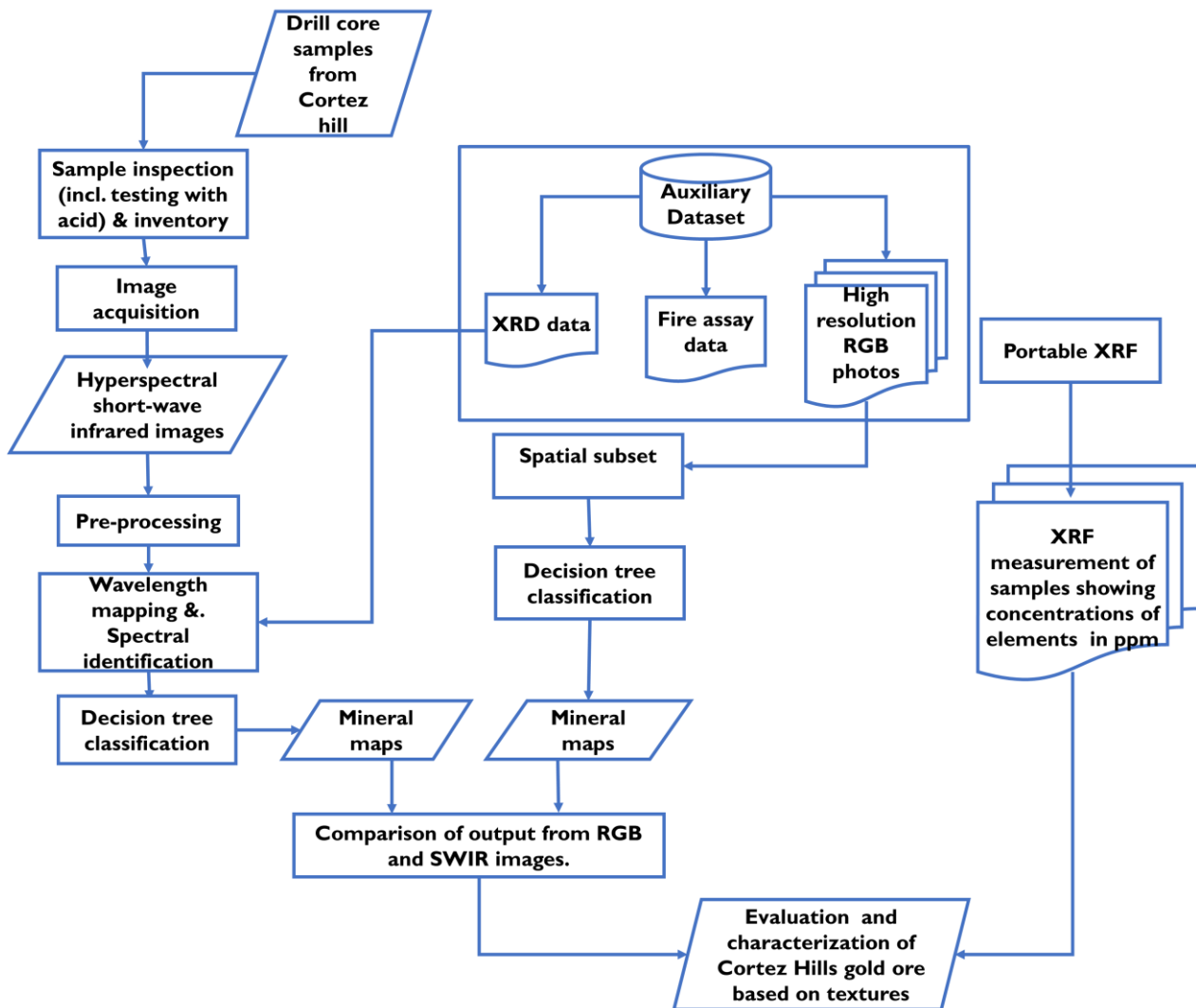
Figure 5: A flowchart showing a summary of the methodology of this research

4. RESULTS

The results of the methods carried out in this research are shown in this chapter. This includes the inventory of textures and lithologies, minerals identified from images of the samples, the mineral maps created using decision tree classifier and the result of the pXRF analysis.

4.1. Texture inventory

4.1.1. Matrix

Matrix or groundmass of a rock body is the smallest or finer grained minerals in which coarser or larger grain materials are embedded or surrounded (Britannica.com, 2011). Figure 3 below shows the type of matrix observed in the samples;

I. A fine-grained matrix occurring as either;
- ✓ Grey to dark grey layered matrix as seen in silty limestone and silty micrite samples (see *Figure 6 (a)*)
- ✓ Homogenous dark grey matrix also in Silty limestone and Silty micrite (*see Figure 6 (b)*) ,
- ✓ Altered reddish matrix as seen in the Calcareous siltstones (*see Figure 6 (c)*),
- ✓ Weathered texture of micrite (*see Figure 6 (g)*).

II. Microcrystalline carbonate matrix as seen in the Dolomite and marble samples (*see Figure 6 (d)*)

III. Porphyritic textures with large crystals in a fined grain matrix: The matrix of the intrusive igneous rocks have observed in the samples were of three types;
- ✓ orange-pinkish matrix with colourless, white and black phenocryst (*see Figure 6 (e)*),
- ✓ white-grey matrix with colourless, white and black phenocryst (*see Figure 6 (f)*,
- ✓ weathered porphyritic texture, the variation in the degree of weathering caused a layering pattern to develop in the sample as seen in sample E264_271m (*see Figure 6 (h)*).

(a)	(b)	(c)	(d)

(e)	(f)	(g)	(h)
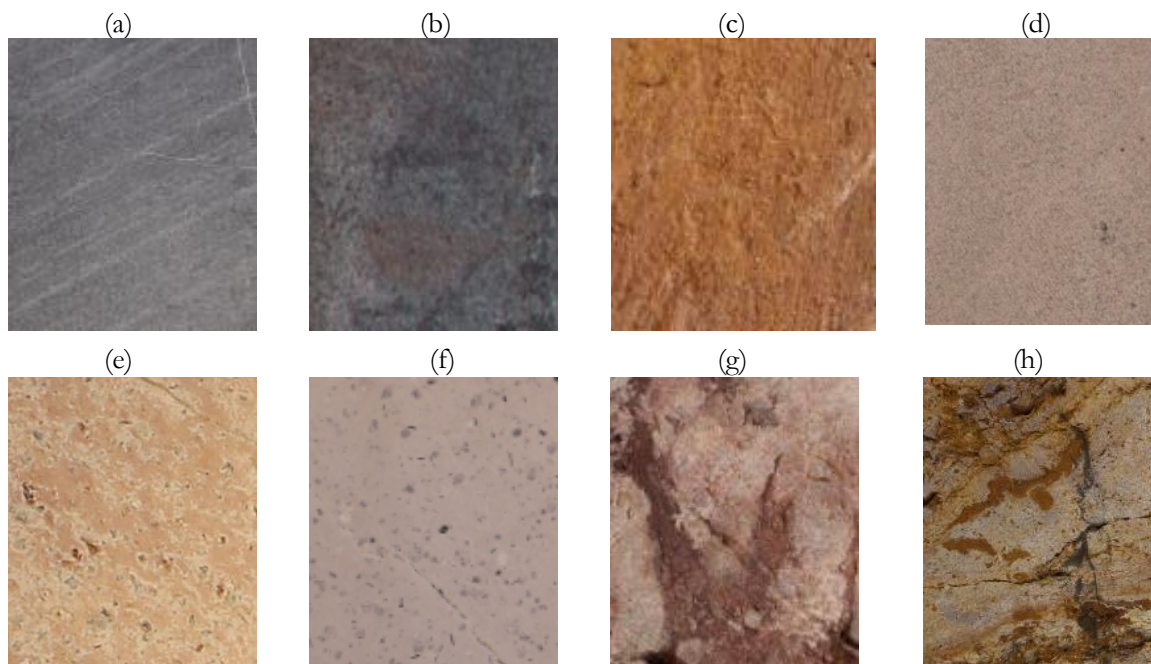
Figure 6: showing textures identified in the samples. (a) layered grey matrix; (b) homogenous dark grey matrix; (c) altered reddish matrix; (d) microcrystalline carbonate matrix, (e) orange-pinkish porphyritic matrix, (f) white-light grey porphyritic matrix (g) weathered micrite texture(sedimentary)) (h). weathered porphyritic texture (igneous)

4.1.2. Veins, layering

Other structures such as veins and layering were found. Veins are geological textures formed when a fracture within a rock body is filled with new rock material either during intrusion of igneous bodies, during metamorphic processes that cause zonation and recrystallization of minerals in metamorphic rocks or by deposition from migrating hot hydrothermal fluids rich in the minerals that are later precipitated and deposited in fractures in the host rock. Layering was also observed in the samples. Layering is characteristic of sedimentary rocks formed by the sequential deposition of sedimentary beds on top of one another and can denote bedding plans or unconformities. It is a useful characteristic in determining the age and depositional environment of sedimentary rock. Displayed in figure 5 below are the types of veins and layering identified in the samples. They include planar veins, deformed/irregular shaped veins, crosscutting veins, as well as layering vein but in a crystalline carbonate matrix

(a)	(b)	(c)	(d)

(e)	(f)	(g)	(h)
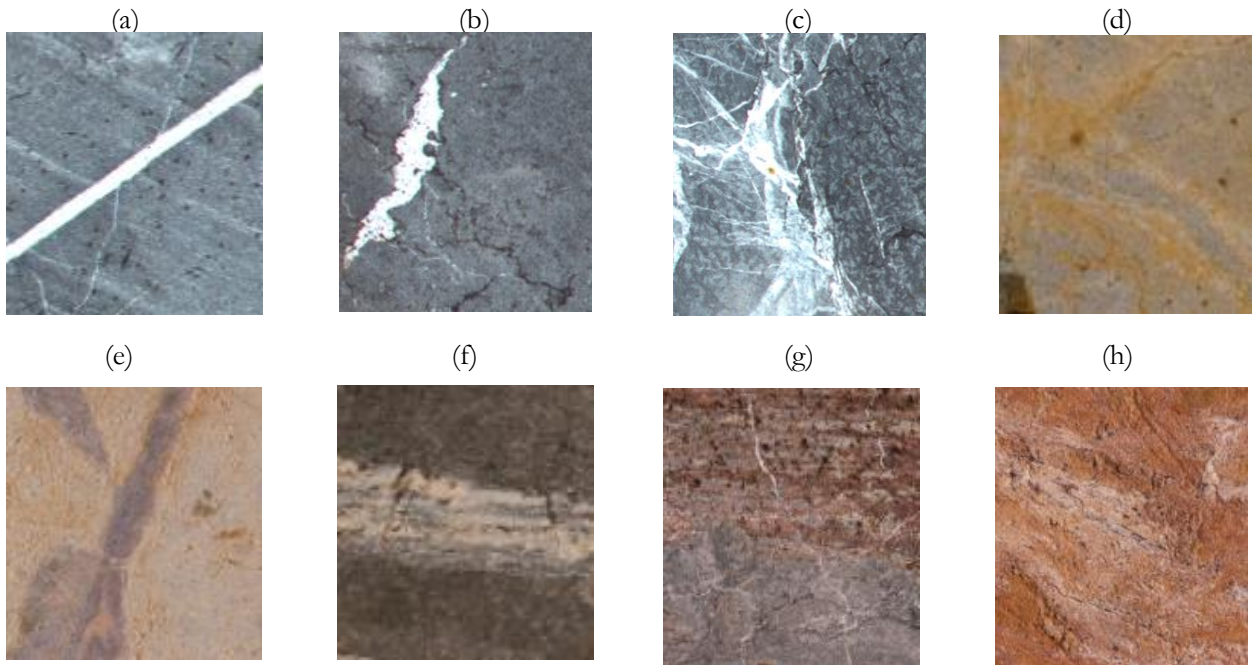
Figure 7: Showing the types of veins and layering and identified from the samples (a) planar vein crosscutting layered matrix; (b) deformed vein in grey matrix; (c) crosscutting veins (d) white mica veins in microcrystalline carbonate matrix, (e) white mica vein in crystalline carbonate matrix (f) layered vein in grey matrix (g)oxidized layering in grey matrix (h) white mica veins in red matrix of calcareous siltstone

4.1.3. Breccias and Clast

These are larger grain clasts from pre-existing rocks hosted within finer grain particles that act as cement The types of breccias and clast observed in the samples include; dark grey breccia in light grey matrix/or powdery white matrix *(Figure 8a),* Pink clast in dark grey mineral matrix *(Figure 8b),* Dark grey matrix with white lens-clasts since in silty limestone at contact with the porphyries *(Figure 8c).*

(a)	(b)	(c)
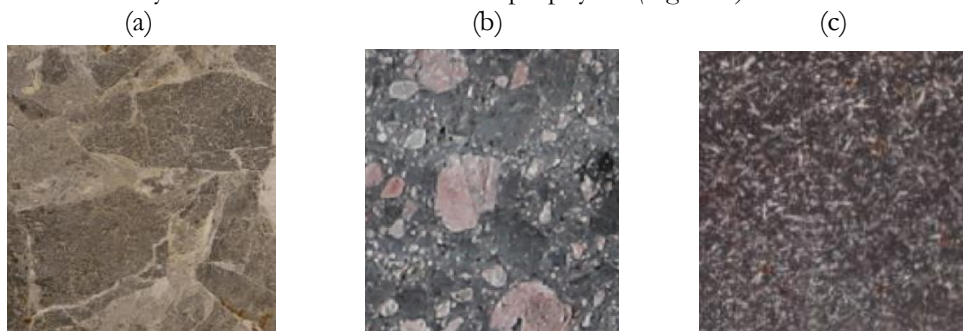
Figure 8: showing identified clastic textures. (i) brecciated texture (ii) round-clasts (ii) lens-clast;

4.2. Sample inventory

The various rock units found in these 3 drill holes include silty limestone, micrite, silty micrite, calcareous siltstone, marble, dolomite, quartz and feldspathic porphyry. In this section, the typical samples of each lithology are described (*see Table 4 for summary of general lithologies and Tables 5,6 and 7 for the description of samples for each drill hole*).

4.2.1. Silty limestone:

Silty limestone is a classification giving to limestone made up of calcite $CaCO_3$ and a high percentage of silt-sized particles. Silt-size particles are between 0.002mm and 0.0063mm; they are usually comprised of quartz, feldspars and micas (mindat.org, 2019). The samples with this classified as silty limestone in the auxiliary data are of three types:

- Silty Limestone with grey minerals that contain carbonates because it reacted to HNO3 acid, layering and + or - vein)(*see Figure 6a*).
- Silty limestone with dark grey contains no carbonates because it didn't react to the acid with no observable layering pattern. For example, E264_500m and sample E264_507m (*see Figure 6b*).
- Silty limestone with len-clast. An example of this is sample E264_264m (*see Figure 6c*).

4.2.2. Calcareous siltstone:

These samples are light grey in colour and fine grained or reddish brown with medium to fine grained minerals. They grey coloured samples appear to have microcrystalline carbonate minerals matrix (see figure 6d). Most samples from E264 have reddish colouration indicating iron oxidation. It is medium to fine-grained with a shaly texture and slightly weathered (*see Figure 7h*). These altered samples possess white layering within their reddish matrix. Examples of this lithology are samples E264_714m and E352_992m.

4.2.3. Micrite and Silty Micrite

Micrite is a mud grade limestone. They are fine to very fine-grained. Samples are grey to dark grey, layered or unlayered while others were reddish brown and highly weathered. The weathered samples did not react to acid when tested. Examples of this lithology are E352_650m for weathered and E352_252m for dark grey.

4.2.4. Dolostone

This is a dolomite rock. It is a sedimentary carbonate rock with dolomite; a magnesium-rich calcium carbonate mineral $(CaMg(CO_3)_2)$ as its dominant carbonate mineral rocks. It can be colourless, white, grey or reddish/pinkish white colour. Two types of dolostone were observed in the dataset; light grey to the light red coloured matrix, for example, sample e352_708m and grey coloured matrix, for example, sample, e297_1198m.

4.2.5. Marble:

An example of this lithology is sample E264_652m and 809m This is a metamorphic carbonate rock formed when sedimentary carbonate rock is subjected to heat and pressure that causes carbonate minerals (usually calcite or dolomite) to recrystallize. A metamorphic rock is classified as Marble when 50% of its constituent volume is made up of carbonate minerals.

4.2.6. Quartz and Feldspathic Porphyry:

Feldspathic porphyries had pink coloured groundmass colour while Quartz porphyries had white coloured groundmass. Weathered samples showed layering due to differences in the degree of weathering. The

feldspar was more weathered because of the lower concentration of quartz, which is more resistant to weathering than feldspar.

4.3.   The acid test for carbonate minerals:

The samples were also tested using nitric acid. The result of the test on samples is displayed in tables 3-6 below. It shows that most of the samples contained carbonate minerals. However, the quartz and feldspar porphyry and the unlayered silty limestone samples also do not react with the acid.

Table 4: Summary of lithologies

Silty Limestone (SL)	Feldspar porphyry (FP)	Quartz porphyry (QP)	Calcareous siltstone (CS)	Marble (MB): White to light grey microcrystalline matrix	Micrite (MI)	Dolostone (DO)
SL-a: Grey and layered fine grained matrix, reactive to acid	**FP-a**: Light grey with white and black phenocryst	**QP-a**: White fine grained matrix with phenocryst	**CS-a**: White, Light grey to light orange crystalline carbonate; reactive to acid		**MI-a**: Grey to dark grey matrix	**DO-a**: oxidized reddish coloured medium grain matrix
SL-b: Homogenous fine grained matrix; not reactive	**FP-b**: Reddish oxidation stain and weathered	**QP-b**: pinkish orange fine grained matrix with phenocryst	**CS-b**: Reddish oxidized medium grained matrix with white veins or layers.		**MI-b**: Weathered and oxidized matrix	**DO-b**: dark grey fine grained matrix
SL-c: Dark grey fine grained matrix with len-clast			**CS-c**: White, Light grey to light orange matrix with len-clast		Silty micrite (**SM**): Grey coloured and layered fine grained matrix	**DO-c**: Light grey and orange fined grained matrix

Table 5: Showing description of samples from drill hole CHUE-264 including the result of fire assay test in ppm and acid test for carbonates.

E-264	Lith	Description	Texture	Weathered /oxidized	Au (ppm)	As (ppm)	Reacts with acid
51m	SL	grey matrix; layered	white vein	No/no	0.0001	-0	Yes
102m	SL	grey matrix; layered,	thin veins	No/no	0.0001	-0	Yes
153m	SL	grey matrix; layered,	fractured, vein	No/no	0.0001	-0	Yes
191m	SL	dark grey, no layering	sigmoidal vein, fractured	no/yes	0.0322	-0	Yes
256m	FP	light grey, porphyritic	-	Yes/no	0.0016	-0	No
264m	SL	white-pink, clast (appears porphyritic)	-	No/no	0.0321	23.9	No
271m	FP	red, orange, highly weathered	-	Yes/Yes	0.0005	-0	No
303m	SL	dark grey matrix	white veins, fractured		0.0303	101	Yes
318m	SL	dark grey matrix	crosscutting white vein,	No/no	0.116	101	Yes
322m	SL	dark grey matrix, conglomerate	white vein, pink clast	No/no	0.116	101	Yes
352m	QP	orange, pinkish-grey; porphyritic	-	No/no	0.0007	-0	Yes
380m	QP	orange, pinkish-grey; porphyritic	red oxidized layer	No/yes	0.0003	-0	No
396m	QP	orange, pinkish-grey; porphyritic	-	No/no	0.0006	-0	No
467m	SL	dark grey with white lens like clast	-	-	0.052	57.6	No
492m	SL	dark grey with white lens like clast	fractured	-	0.162	56.2	No
500m	SL	dark grey	fractured	No/no	1.175	80.5	No
502m	SL	dark grey, reddish stain	red vein	Yes/yes	1.175	80.5	No
506m	SL	dark grey, reddish stain, layering		No/yes	0.379	80.5	No
507m	SL	dark grey	White vein and banding	No/no	0.379	80.5	No
528m	CS	reddish brown		Yes/yes	1.045	93.6	No
578m	CS	reddish	White banding	Yes/yes	0.0127	114	Yes (Mild)
581m	CS	reddish and pink; white layering	White banding	No/yes	0.0127	114	No
606m	CS	reddish and pink; white layering	-	Yes/yes	0.0106	292	
652m	MB	grey rock,	fractured	no/yes	0.0764	27.8	No
714m	DO	reddish, orange pink and white layered	-	-	0.0143	1100	Yes (Mild)
760m	CS	reddish, orange	-	yes/yes	0.0009	126.5	No
809m	MB	white and grey	-	No/no	0.0003	219	No

Table 6 Showing description of samples from drill hole CHUE-297 including the result of fire assay test in ppm and the acid test for carbonates.

E-297	Lith	Description	Structure	Weathered /oxidized	Au (ppm)	As (ppm)	Reacts with acid
51m	SM	grey matrix, layered	-	no/no	0.0001	-0	Yes
103m	CS	White to pink matrix	-	no/no	0.0002	-0	Yes
153m	SM	grey matrix, layered	white vein	no/no	0.0001	-0	Yes
203m	SM	grey matrix, layered	-	no/no	0.0573	-0	Yes
248m	SM	grey matrix, layered	fractured	no/no	0.0001	-0	Yes
307m	SM	grey matrix, layered	white vein, fractured	no/no	0.0001	-0	Yes
357m	QP	white matrix; porphyritic: white phenocryst	-	no/no	0.0001	-0	No
404m	QP	light grey matrix, porphyritic: white and black phenocryst	-	no/no	0.0042	-0	No
458m	QP	light grey, porphyritic: white and black phenocryst	-	no/no	0.109	-0	No
503m	QP	white rock; porphyritic: colourless, white and black phenocryst	-	no/no	0.327	-0	No
551m	QP	white rock; porphyritic: colourless, white and black phenocryst	fractured	no/no	0.0007	-0	No
601m	QP	white rock; porphyritic: colourless, white and black phenocryst	-	-	0.0018	-0	No
658m	QP	white rock; porphyritic: colourless, white and black phenocryst	fractured	-	0.0001	-0	No
702m	QP	white rock; porphyritic: colourless, white and black phenocryst	-	-	0.0001	-0	No
752m	MI	Dark grey with white veins	Fractured	-	0.058	-0	Yes
796m	MI	Dark grey	-	-	0.722	-0	No
858m	QP	white rock; porphyritic: colourless, white and black phenocryst	fractured	no/no	0.0017	137.5	No
902m	MI	dark grey	-	no/no	0.0455	104	Yes
949m	QP	dark grey, not porphyritic, contact between porphyry and micrite	fractured, pink veinlet	no/no	0.0008	68.5	No
1007m	QP	pink, porphyritic: red white and black phenocryst			0.0007	23.2	No
1052m	MI	dark grey	white stockwork veins, fractured	no/no	0.0001	-0	Yes
1104m	QP	light grey, colourless and black phenocryst		no/no	0.0001	-0	No
1152m	CS	white and black	white veins	no/no	0.0001	-0	Yes
1198m	DO	Grey matrix	fractured		0.0002	-0	Yes (Mild)

Table 7 Showing description of samples from drill hole CHUE-352 including result of fire assay test in ppm

E-352	Lith	Description	Structure	Weathered/oxidation	Au (ppm)	As (ppm)	Reacts with acid
51m	MI	light grey matrix, large dark grey breccia	brecciated, white veins	No/no	0.0001	nm	Yes
97m	CS	white matrix, reddish stains	Small grey breccias	Yes/yes	0.0001	-0	Yes
152m	CS	light grey to pink matrix; reddish stain; evenly distributed clast throughout matrix	small black clast	No/yes	0.0004	-0	-
203m	MI	dark grey; layered; with reddish stain on vein	White vein, fractures	no/yes	0.0002	-0	Yes
252m	MI	grey matrix	White stockwork veins	No/no	0.0002	-0	Yes
305m	QP	white rock; porphyritic: colourless, white and black phenocryst	-	no/no	0.0001	-0	No
350m	QP	white rock; porphyritic: colourless, white and black phenocryst	-	no/no	0.0001	-0	No
405m	SM	grey matrix, layered, reddish stain	White vein, fractures	Yes/yes	0.0143	-0	Yes
448m	QP	pink matrix; porphyritic: colourless, white and black phenocryst	-	-	0.0001	-0	No
500m	CS	dark brown matrix, small white clast evenly distributed throughout matrix	fractures		0.0894	-0	No
554m	SM	grey matrix, layered	-	-	0.233	72.6	Yes
600m	MI	reddish brown	Fractures	Yes/yes	0.421	106	No
650m	MI	Reddish brown	fractures	Yes/yes	0.365	154.5	No
708m	DO	light grey to light red	Fractures	-	0.0048	-0	Yes (Mild)
798m	DO	light grey to light red	Veins, Fractures	No/no	0.0052	-0	Yes (Mild)
851m	CS	grey to light orange	Vein, Fractures	No/no	0.0028	-0	Yes (Mild)
901m	CS	light grey to orange,	Vein, fractures	No/no	0.0004	-0	Yes (Mild)
946m	CS	light grey to orange, vein with reddish stain		No/yes	0.0002	-0	Yes
992m	CS	light grey to light pink	Veins	No/no	0.0015	-0	Yes
1050 m	CS	light grey to light pink	Veins	No/no	0.0001	-0	Yes
1205 m	CS	light grey	-	-	0.0001	-0	Yes

4.4. Mineral identification

This section shows the minerals that were identified using spectral inspection, wavelength maps and band ratios of the images, and comparison with G-Mex documentation and United State Geological Survey spectral library of minerals. This process was also informed by the minerals already identified in previous works was carried out by Dalm (2017) and Bevan (2018). The mineral classes identified to coincide with the minerals already identified from the available XRD data and Bevan (2018)'s research on a subset of the drill cores. The mineral classes, as well as mineral mixtures identified, are listed below:

4.4.1. Spectral mineral classes:

The mineral classes identified from the samples and used for the classification of SWIR images into mineral maps are listed below. Their image spectrum compared with the USGS reference spectrum for each of the images is displayed in Figure 9:

a) Calcite & Dolomite ($CaCO_3$ & $CaMg(CO_3)_2$):
   Calcite is a calcium carbonate mineral ($CaCO_3$) while dolomite is a carbonate mineral like calcite but with magnesium in its molecules ($CaMg(CO_3)_2$). Calcite its CO_3^{2-} absorption feature at 2320 - 2360nm while dolomite has its absorption feature at shorter wavelengths of 2300-2320nm with a second feature at 2100 to 2160nm. Calcite spectrum is displayed in Figure9a while Dolomite's is displayed in Figure 9c.

b) Magnesium Chlorite: This is the magnesium rich variant of Chlorite. Chlorite is a common alteration product of mafic minerals and an indicator of low-grade metamorphism. Magnesium chlorite has its deepest absorption feature at 2300 to 2320nm and the second deepest at 2240 to 2260nm and a third at 2380nm. This mineral was found in un-oxidized calcareous siltstone samples.

c) Tremolite & Talc: Tremolite is a mineral within the amphibolite-actinolite series formed from the contact metamorphism of calcium carbonate rocks. It is commonly associated with Calcite Dolomite, Talc , Diopside and has a chemical formula $Ca_2(Mg;Fe^{2+})_5Si_8O_{22}(OH)_2$ (Anthony, Bideaux, Bladh, & Nichols, 2010; Webmineral.com, 2012). Talc and Tremolite have overlapping diagnostic features at 2300-2320nm and at 2340-2400nm. These two minerals can be separated based on a third absorption feature Talc has in 1850-1910nm. However, for this research separating these two classes didn't improve the classification.

d) Epidote: This is a sorosilicate mineral with calcium and iron cations in its crystal structure. It is a metamorphic mineral indicative of low to moderate grade metamorphism. It has a chemical formula $\{Ca_2\}\{Al_2Fe^{3+}\}(Si_2O_7)(SiO_4)O(OH)$. This mineral was found in marble sample E264_809m.

e) White Micas & Clays: These are phyllosilicate minerals with aluminium hydroxyl (Al-OH) bonds in their molecules. They have a chemical formula $KAl_2(AlSi_3O_{10})(OH)_2$. This class includes muscovite illite and clays minerals like montmorillonite. The vibrational bond that exhibits itself as a distinctive feature around the 2208nm range with another shallow feature at 2340nm for micas (Scott & Yang, 1997; Swayze et al., 2014). The minerals identified in this range included (i) white micas; which were delineated into classes based on the position of 2208nm and the second absorption feature into 3

subclasses; 2200-2205nm. 2205-2210nm and 2210-2220nm, (ii) Montmorillonite which doesn't have a distinct 2340nm absorption feature and (iii) a mixed class of clays and carbonates.

f) Phengite: Phengite is a phyllosilicate mineral, a variety of muscovite with its deepest absorption feature at longer wavelengths of 2220-2240nm. The shift of the feature into longer wavelengths is caused by lower concentrations of Aluminium ion in the lattice of the mineral as Al is substituted for by Silica and Mg, Fe cations (Clark, 1999; Swayze et al., 2014).

g) Kaolinite: Kaolinite is also a phyllosilicate mineral with a chemical formula $Al_2(Si_2O_5)(OH)_4$. It has a similar aluminium hydroxyl bonds absorption feature at the same wavelength range with other clay minerals like montmorillonite and with white mica minerals like illite and muscovite. However, for kaolinite, the deepest absorption feature appears as a distinctive doublet feature in the 2208nm and 2160nm (not as deep as the 2208nm feature).

h) Mixed classes:

✓ Kaolinite (+white mica) mixture: The spectral of this class has a double feature in the same range as kaolinite but the second feature of the doublet is shallow and, in some case, almost non-existent, indicating it is either kaolinite with low crystallinity or it is not a pure sample of kaolinite.

✓ Mixed class 1 (Grey mineral mixture): This is an unclassified mineral with very low reflectance. It is typically grey to dark grey colour with noisy spectra and reflectance value less than 0.1. However, it has a shallow feature at 2290nm, which may be due to the presence of minerals with carbonate or Magnesium hydroxyl ions in the mixture. Otherwise, this mineral lack any diagnostic feature in the SWIR range. They react with acid signifying the presence of carbonates.

✓ Mixed class 2 (carbonate mixed with clay and white mica):
This mineral class has a mixture of carbonate and white mica mineral mixture. It has its deepest absorption feature between 2309nm, and 2320nm, sometimes this feature may occur as a doublet at these two ranges, with a second shoulder feature at 2208- 2214nm.

✓ Mixed class 3 (clay mixed with carbonate):
This mineral class is a mixture of carbonate and Al-OH minerals. It has its deepest absorption feature between 2309nm, and 2320nm, sometimes this feature may occur as a doublet at these two ranges it has a second shoulder feature at 2208- 2214nm and in some samples, this occurs as the kaolinite doublet feature.

✓ The optional 'Low reflectance light grey mineral' class:
This class was defined using an albedo image to highlight white pixels representing thins veins within dark grey samples. These pixels appear light grey and exhibit higher reflectance but have the same spectral characteristics as mixed class1.
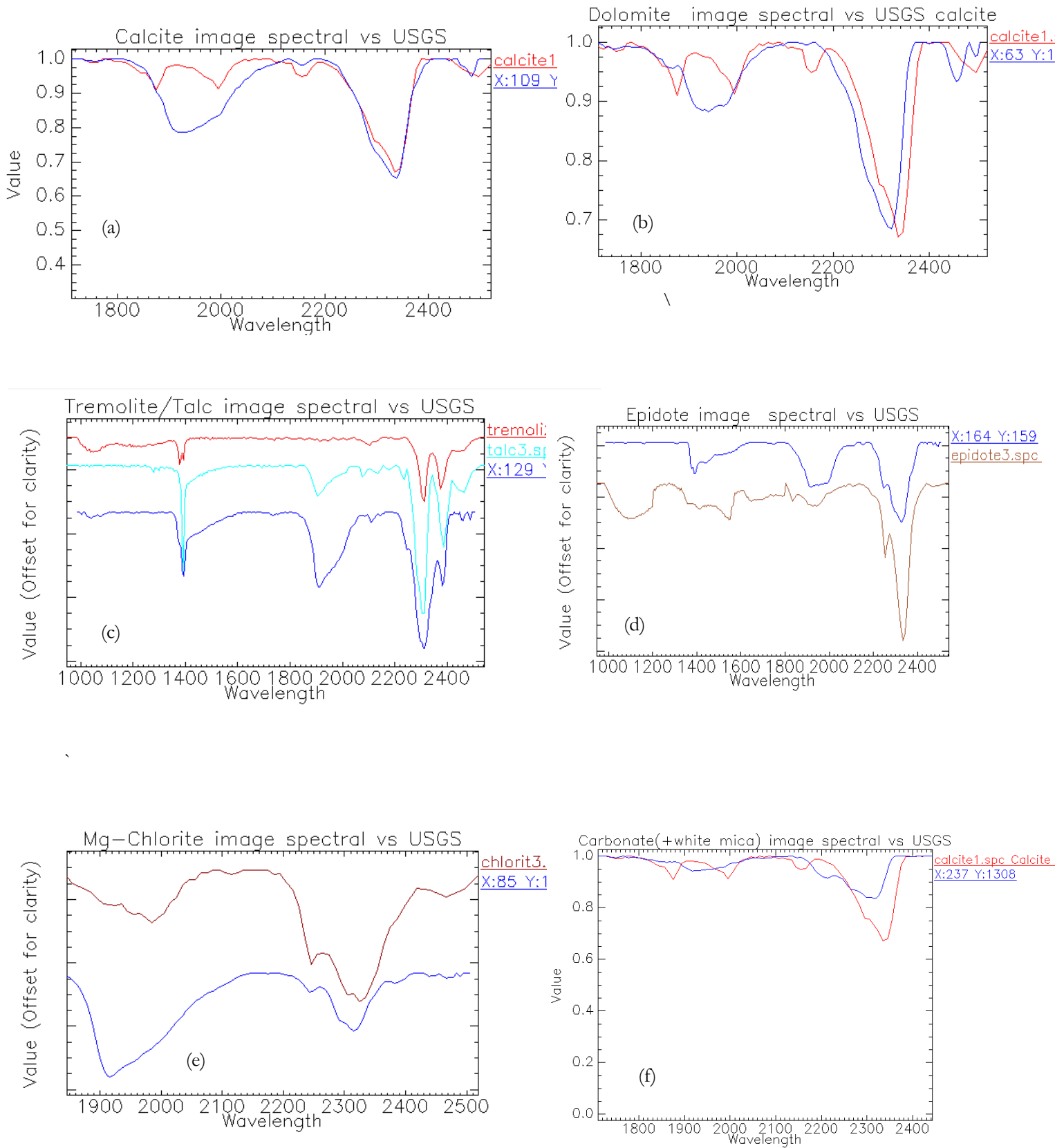
Figure 9: Spectral plot of calcite, dolomite, tremolite, epidote Mg-chlorite and mixed class 2 identified from image spectral (shown in blue) and USGS spectral.
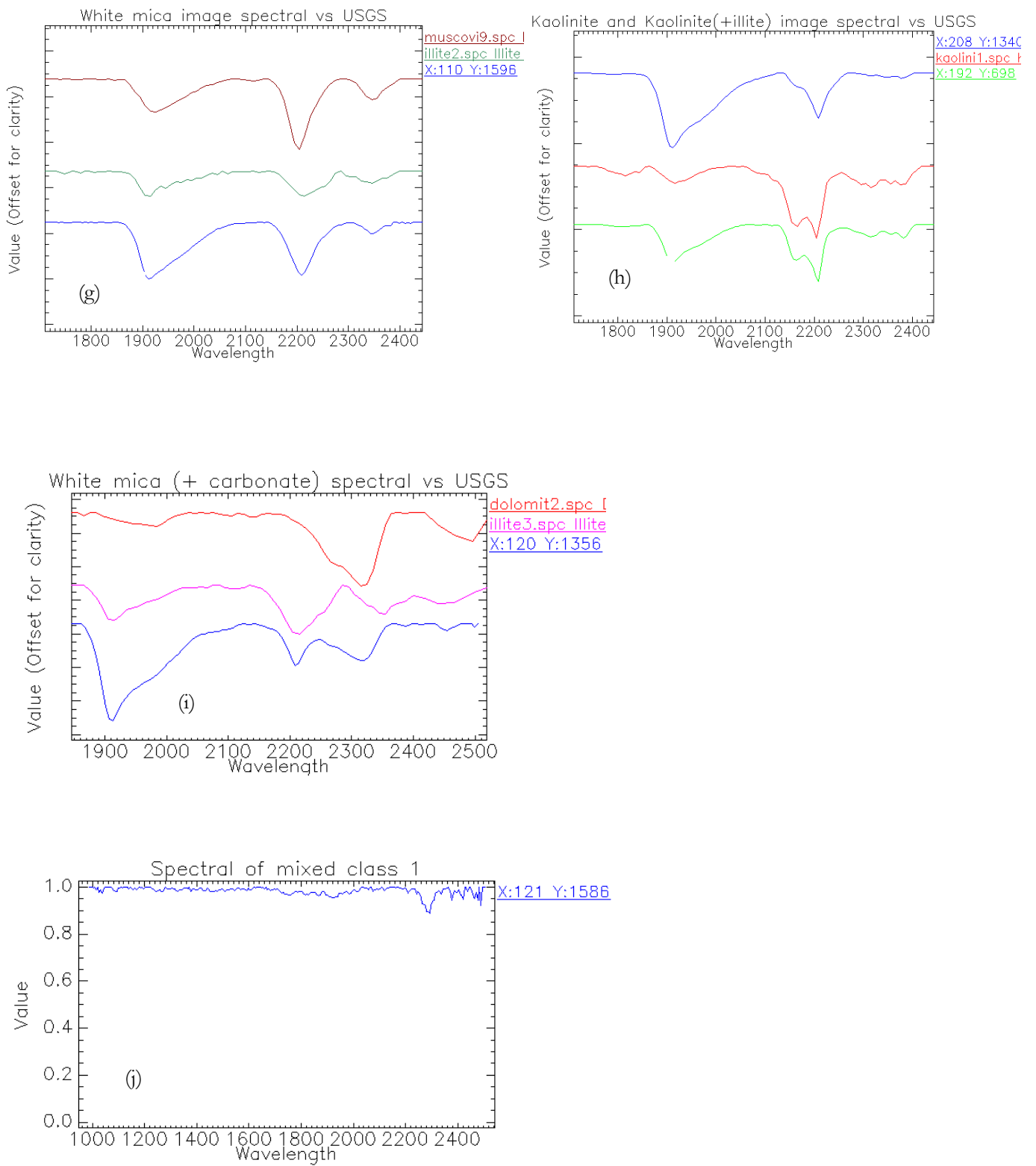
Figure 10: Spectral plot of white micas (g), kaolinite and kaolinite mixed with white mica (h); mixed class 1(j) and mixed class 2 (i) identified from image spectral (shown in blue) and USGS spectral.

4.5. Hyperspectral SWIR mineral maps

The minerals maps from the three drill holes are displayed in this section, At the end of this section, a table showing the samples in relations to their depth can be seen (*see Table 18*)

4.5.1. CHUE-264
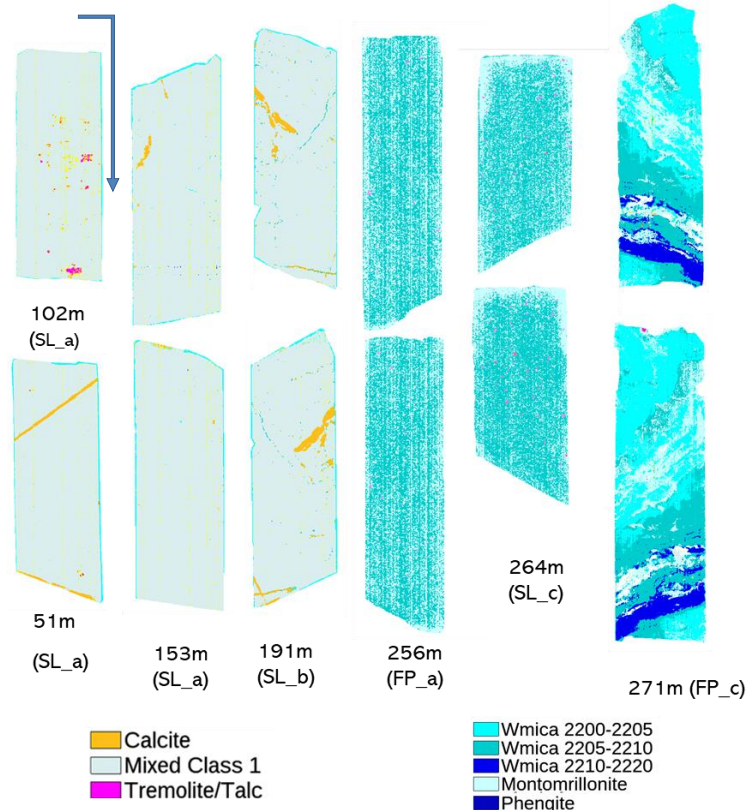
Figure 11: Mineral maps from Decision Tree Classification of SWIR images for samples E264_51m to 271m.
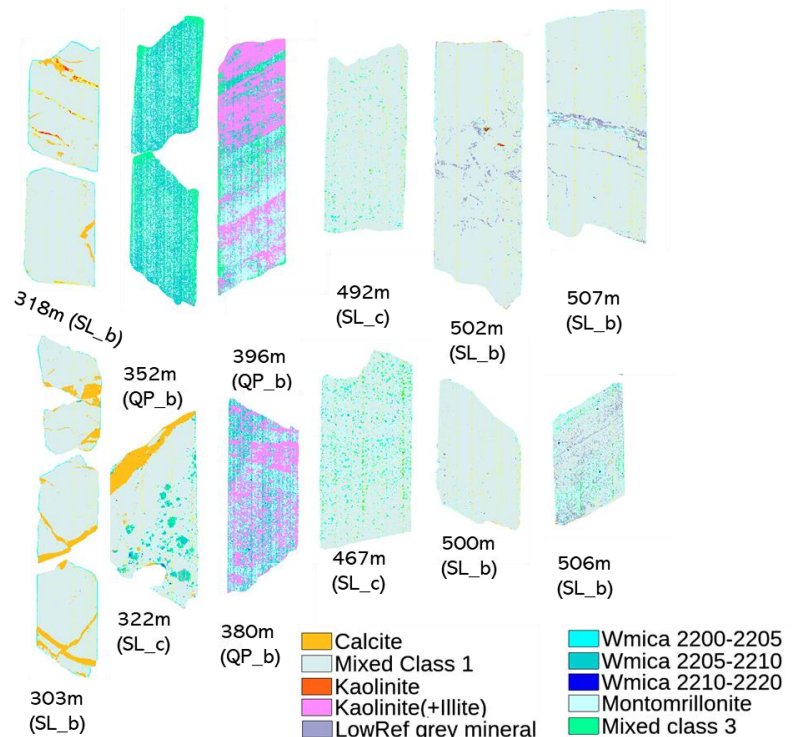
Figure 12: Mineral maps from e264m-303m to 507m created using decision tree classification of SWIR images.
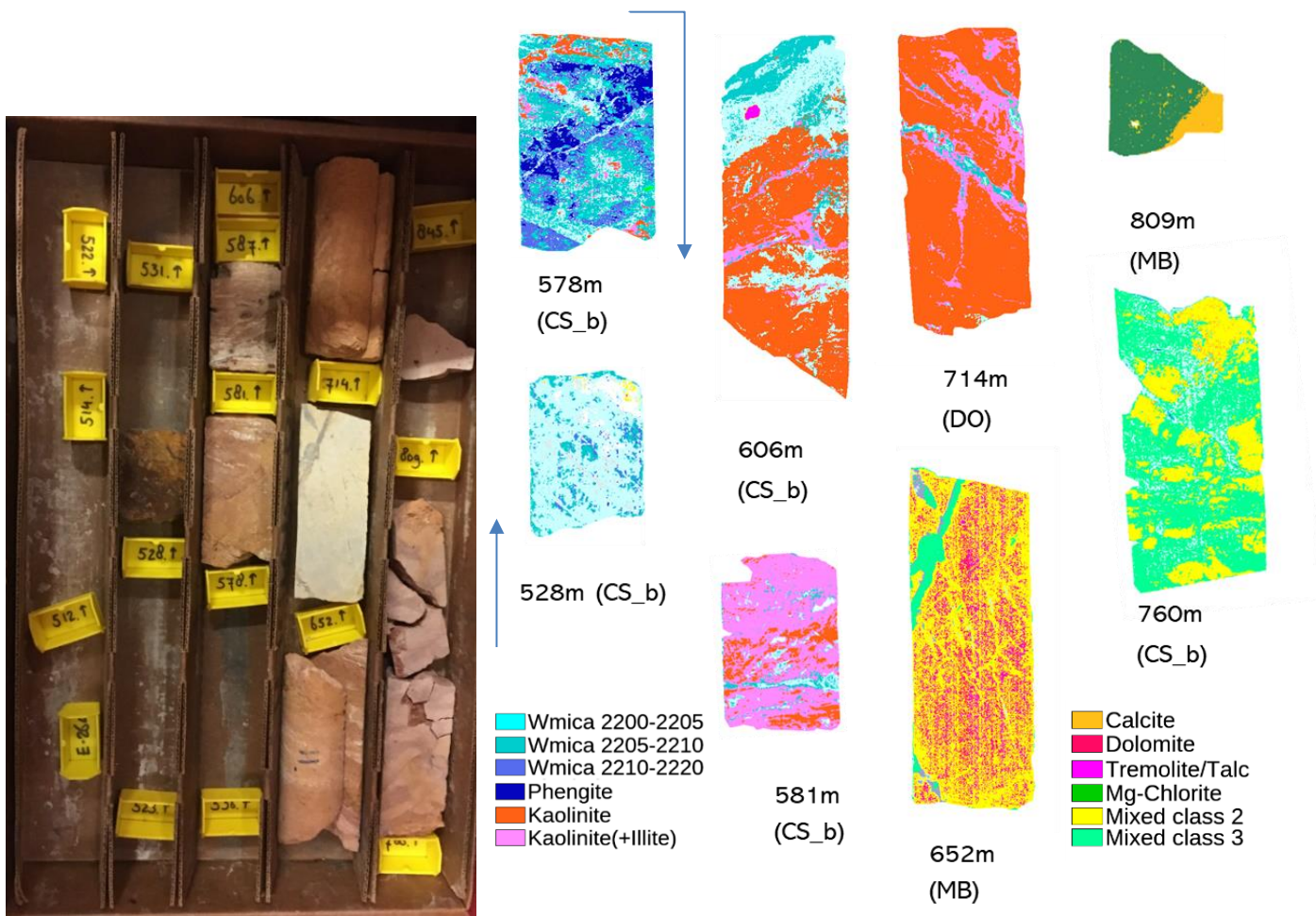
Figure 13: Mineral maps from decision tree classification of SWIR images for sample E264_538m to 760m.

4.5.2. CHUE- 297

The minerals map created from the samples from drill hole CHUE-297 is displayed in Figure 14.
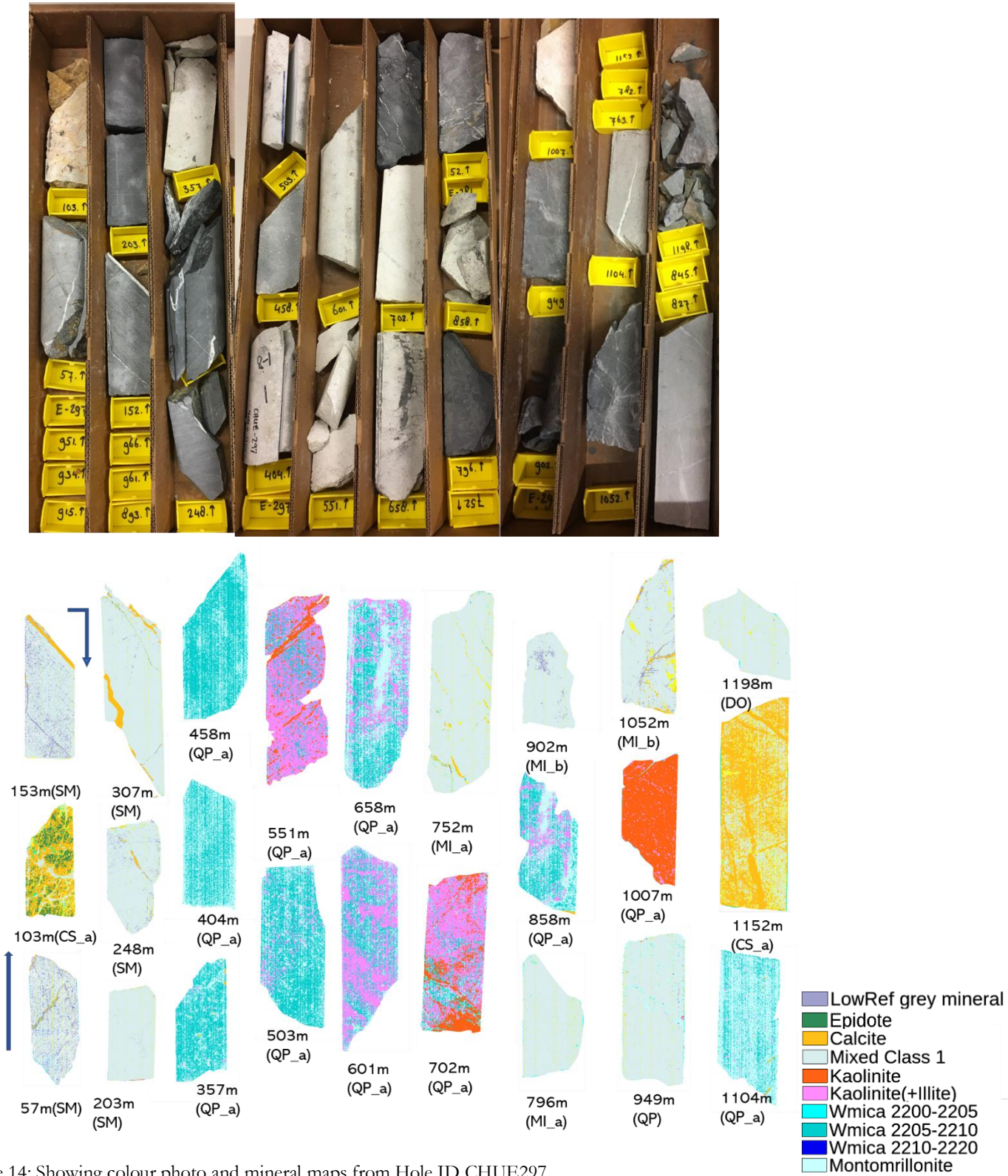
Figure 14: Showing colour photo and mineral maps from Hole ID CHUE297

4.5.3. CHUE-352

The minerals created from drill hole CHUE_352 are displayed in Figure 15:
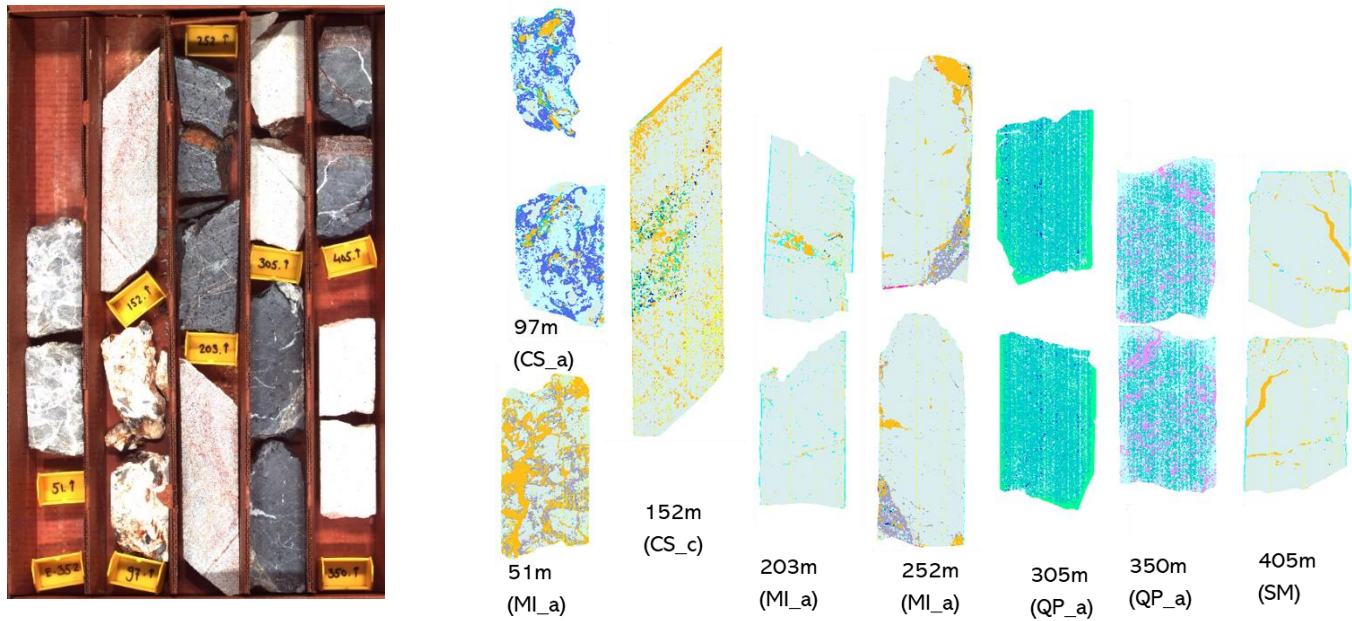
Figure 15: Mineral maps from of CHUE- 352 for samples 51m to 405m
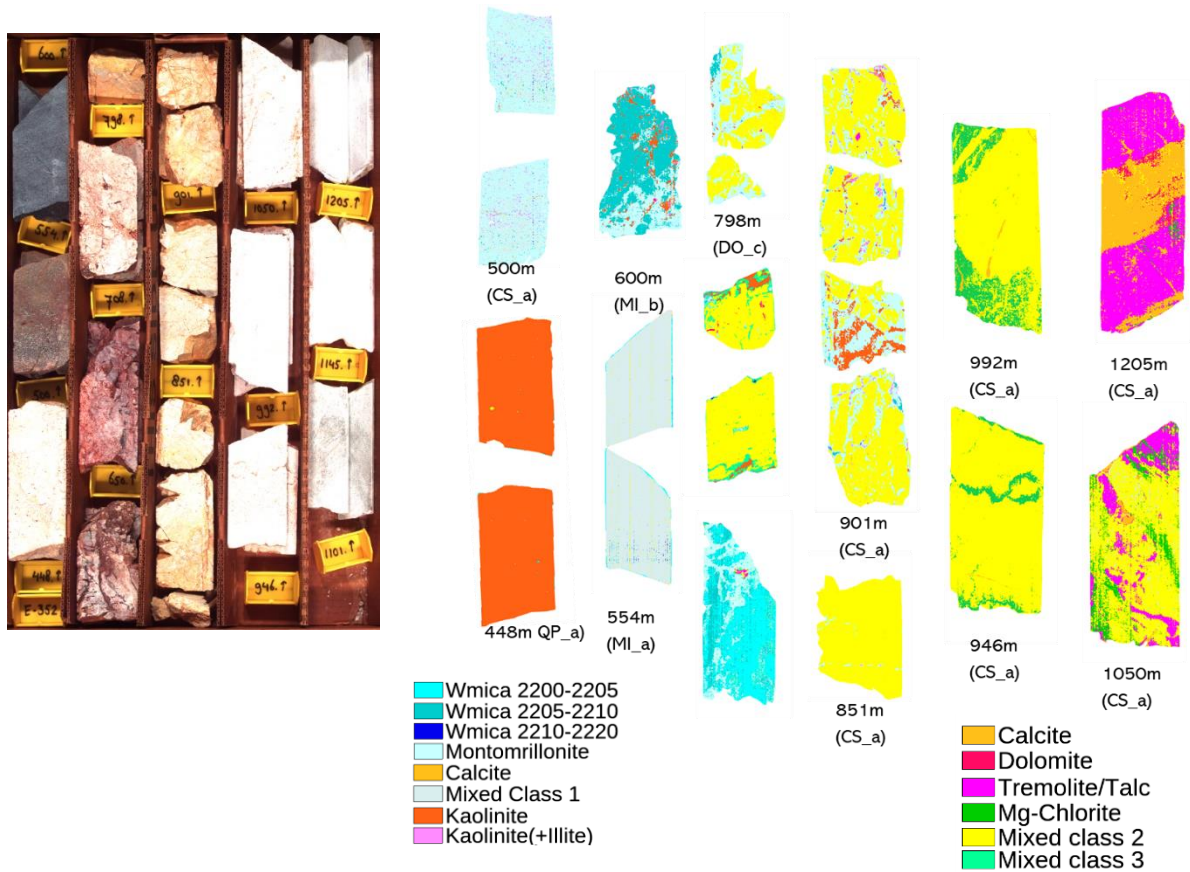
Figure 16: Mineral maps from of CHUE- 352 for samples 448m to 1205m

4.6. RGB classified maps using decision tree

The high-resolution RGB images of the samples were classified using the decision tree classifier. The bands used for classification include blue band, green band and the red band as band 1, 2 and 3 respectively. The maps highlighted the textures in the samples adequately. They classified RGB images of the three drill holes are displayed in Figures 17, 18. The images where classified into 5 classes which were delineated in the decision three based on the values of the classes in the three bands.

CHUE-264

CHUE-297

Legend:
- White mineral
- Dark grey mineral
- Light grey mineral
- Orange mineral
- Reddish brown mineral
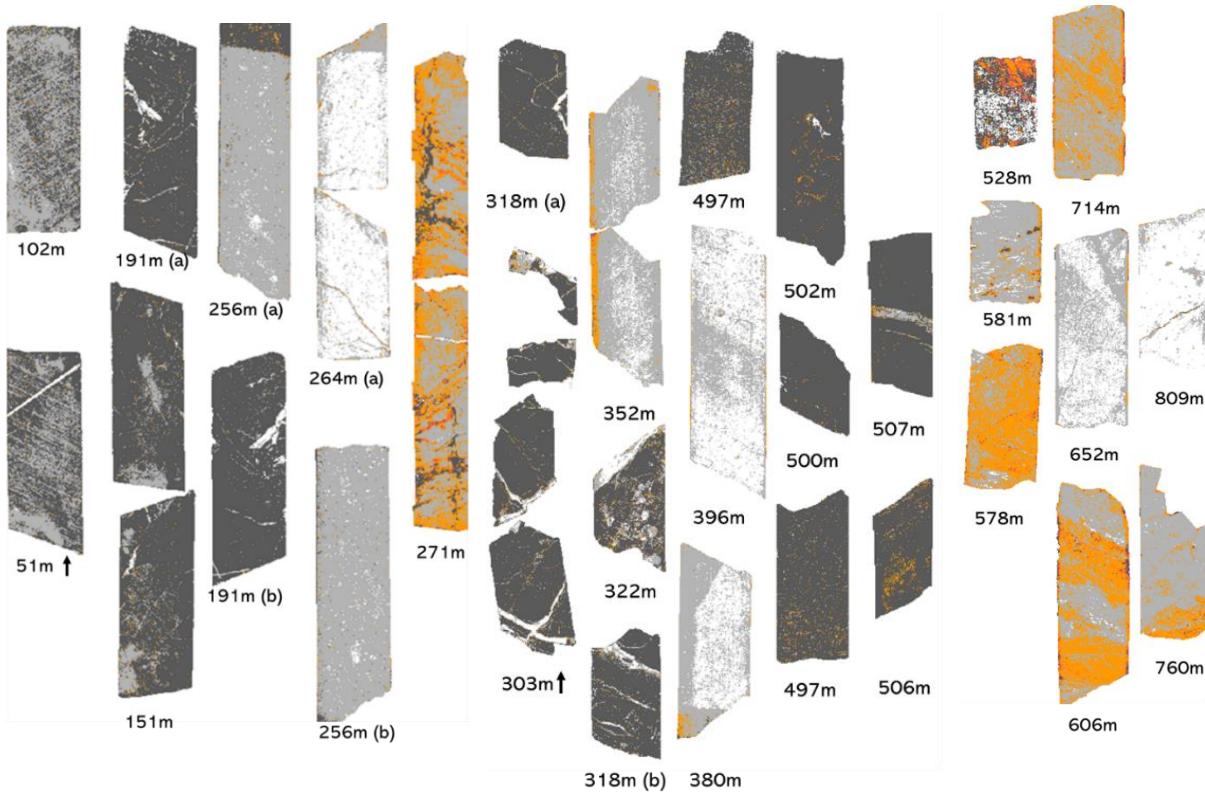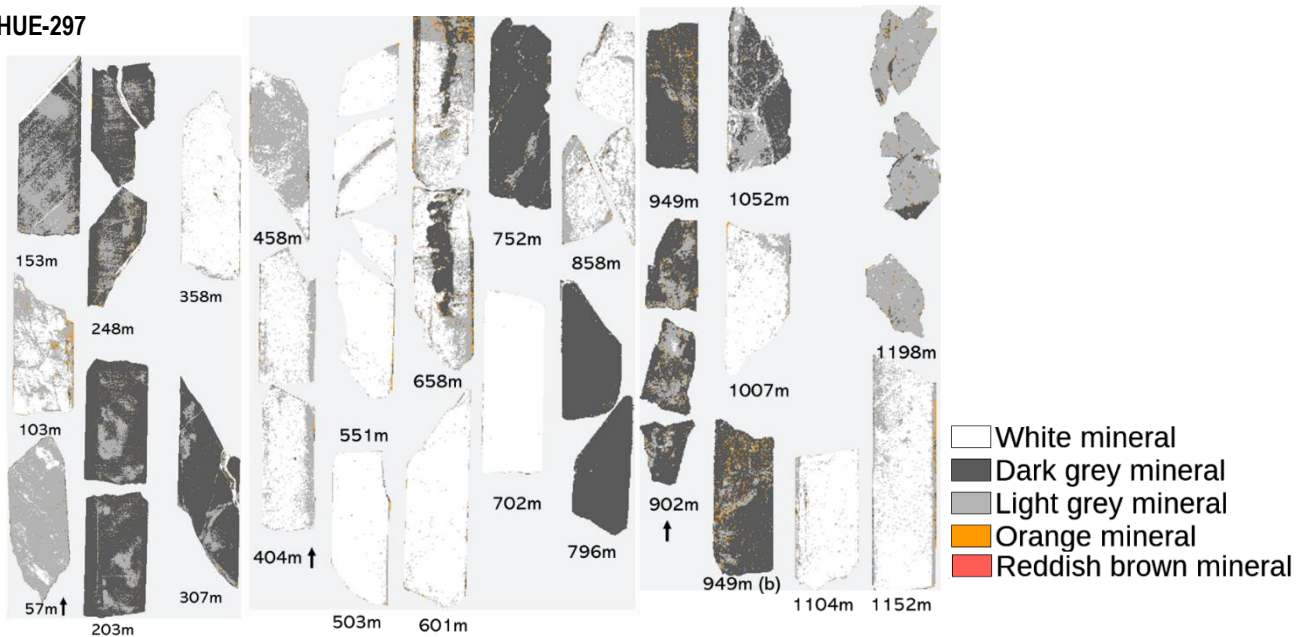
Figure 17: Showing classified RGB photos of CHUE-264 and CHUE-297

CHUE-352
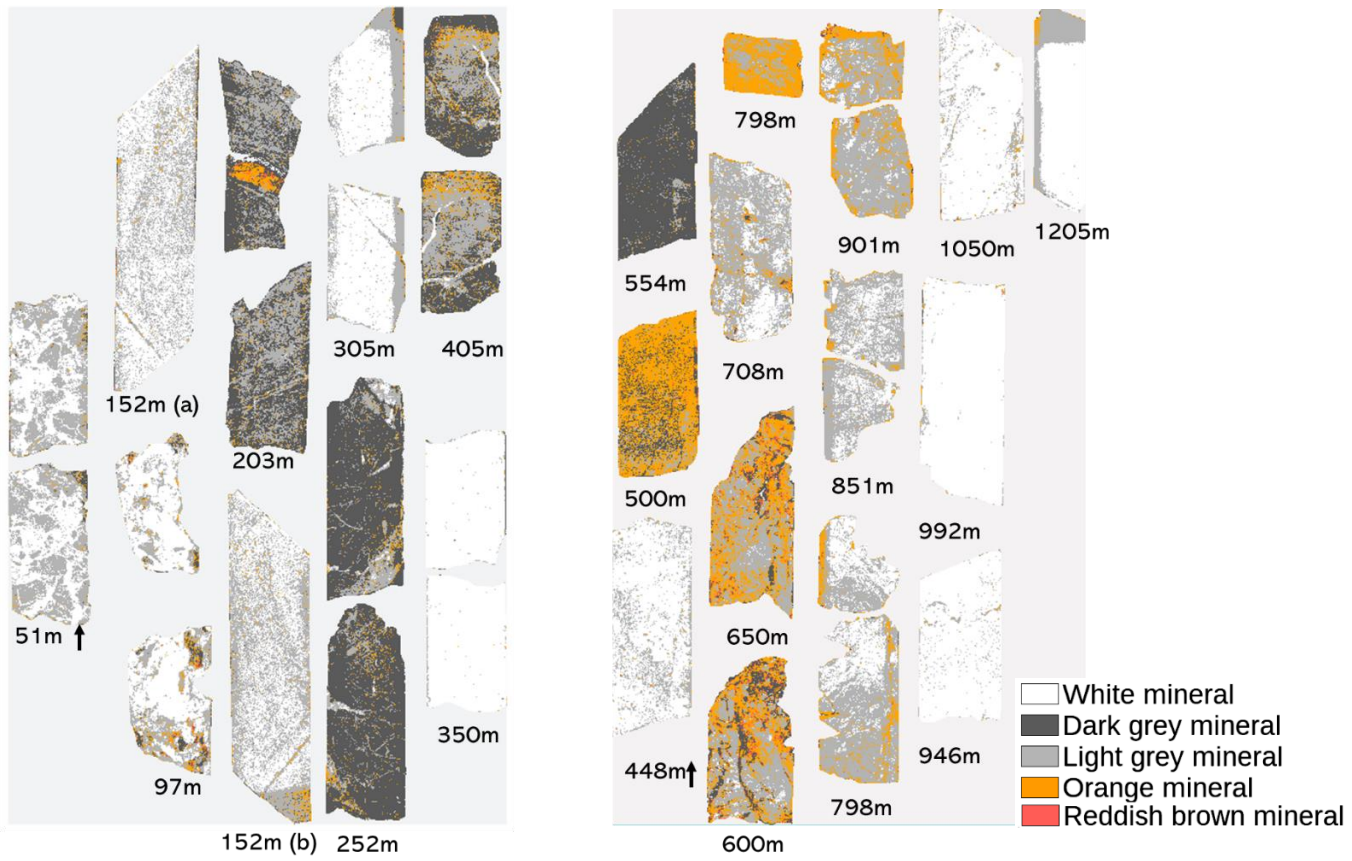
Figure 18: Showing classified RGB photos of CHUE-352

Table 8: Showing mineral maps in relation to depth for the 3 drill holes. The table also shows mineralised samples with depth. Green colour is for samples with high concentration of gold and cyan colour is for samples suspected to contain gold (see section 5.4.2.2). Yellow colour is for samples identified by FA to be mineralized.

E-264

E-264	Sample	Lith	XRF	FA
51m		SL	cyan	
102m		SL		
153m		SL	cyan	
191m		SL	cyan	
256m		FP		
264m		SL		
271m		FP		green
303m		SL		green
318m		SL		green
322m		SL	cyan	
352m		QP		
380m		QP		
396m		QP		
467m		SL		
492m		SL		yellow
500m		SL		yellow
502m		SL	green	yellow
506m		SL		yellow
507m		SL	green	yellow
528m		CS	cyan	yellow
578m		CS		
581m		CS		
606m		CS		
652m		MB		
714m		DO	cyan	
760m		CS		
809m		MB	cyan	

E-297

E-297	Sample	Lith	XRF	FA
51m		SM		
103m		CS	cyan	
153m		SM		
203m		SM	cyan	
248m		SM	cyan	
307m		SM		
357m		QP		
404m		QP		
458m		QP		
503m		QP		yellow
551m		QP		
601m		QP		
658m		QP		
702m		QP		
752m		MI		
796m		MI	green	yellow
858m		QP		
902m		MI		
949m		QP		
1007 m		QP		
1052 m		MI	cyan	
1104 m		QP		
1152 m		CS		
1198 m		DO		

E-352

E-352	Sample	Lith	XRF	FA
51m		MI	cyan	
97m		CS		
152m		CS		
203m		MI	cyan	
252m		MI		
305m		QP		
350m		QP		
405m		SM	cyan	
448m		QP		
500m		CS		
554m		SM	green	yellow
600m		MI	green	yellow
650m		MI		yellow
708m		DO	cyan	
798m		DO		
851m		CS		
901m		CS	cyan	
946m		CS		
992m		CS		
1050 m		CS		
1205 m		CS	cyan	

Legend:
- Wmica 2200-2205
- Wmica 2205-2210
- Wmica 2210-2220
- Montomrillonite
- Phengite
- Calcite
- Mixed Class 1
- Mixed class 2
- Mixed class 3
- Kaolinite
- Kaolinite(+Illite)
- LowRef grey mineral
- Dolomite
- Mg-Chlorite
- Tremolite/Talc
- Epidote

4.6.1. XRF measurement

The results of pXRF measurements can be seen in Appendix 2,3 and 4. However, Tables 9, 10 and 11 displayed below show a pre-processed result of the XRF measurements to remove erroneous measurements. The measurements displayed were the result of averaging of spot measurements carried out on the flat surfaces of the samples, which were also the surfaces imaged. It shows the concentration of gold and arsenic in ppm as well as the error in measurement.

High concentrations of Au are highlighted in green. Au measurements typically had error values of $\pm$ 4ppm to $\pm$6ppm while As typically had error values of $\pm$ 3ppm to $\pm$4ppm Au. Measurement results with values of the mineral below the measurement error were replaced with **LTε** meaning "less than error". For the purpose of this research with the limitation of the measuring device, this value was considered to represent the absent of gold. More detailed results showing the actual values of measurement less than the measured error can be seen in Appendix

The XRF result shows a general trend of higher concentration of gold in the samples compared to those of the fire assay test, though with high error values in some case higher than the measured concentration

The result for the XRF measurements is listed in Tables 7, 8 and 9 below shows Au and As concentrations in parts per million, while Fe Ca and Si are shown in weight percent.

For CHUE-264; samples e264_271m, 303m, 318m, 502m, 507m, and 652m all had Au values higher than 11ppm in their veins. Values measured below this threshold with low error together with the presence of arsenic were taken as in indication of the presence of gold. For CHUE-297, only sample E297_796 was above the 11ppm threshold, with an Au value of 22.40ppm. For CHUE-352, samples E352_ 554m, 600m had values above 11ppm. Most samples of CHUE-297 had values lower than the detection limit and their measurement error. These included all quartz porphyries in drill hole CHUE-297. So, they were considered as unmineralized.

E264

Table 9: Result of XRF measurement of samples from CHUE 264. High values of gold shown in green. **LTε** = values below the device measured error.

CHUE-264	Lithology	Matrix					Vein					breccia/clasts				
		Au	Au error	As	As error	Acid	Au	Au err	As	As err	Acid	Au	Au error	As	As error	Acid
51	SL	6.33	5.42	3.18	3.16	Yes	LTε	4.94	2.91	3.27	Yes	-	-	-	-	-
102	SL	5.19	5.09	2.03	3.21	Yes	-	-	-	-	Yes	-	-	-	-	-
153	SL	6.77	5.29	5.98	3.13	Yes	7.83	5.46	10.22	3.43	Yes	-	-	-	-	-
191	SL	LTε	4.97	14.87	3.62	Yes	6.12	5.69	24.90	4.30	Yes	-	-	-	-	-
256	FP	LTε	4.19	3.35	3.51	No	-	-	-	-	-	-	-	-	-	-
264	SL	LTε	4.29	16.98	4.42	No	-	-	-	-	-	-	-	-	-	-
271	FP	LTε	4.67	217.70	8.58	No	14.93	5.84	352.98	11.31	-	-	-	-	-	-
303	SL	13.24	5.62	109.11	6.77	Yes	12.63	5.81	64.19	5.47	Yes		-	-	-	-
318	SL	6.38	5.23	66.89	5.76	Yes	11.30	5.52	20.20	3.90	Yes	-	-	-	-	-
318b		5.01	4.45	75.61	5.41	Yes	6.99	4.86	51.57	4.84	Yes	-	-	-	-	-
322	SL	8.37	5.28	127.51	7.24	Yes	6.14	5.11	29.95	4.32	Yes	LTε	4.89	83.62	6.53	Yes
352	QP	LTε	4.14	7.96	3.62	No	-	-	-	-	-	-	-	-	-	-
380	QP	LTε	4.07	13.78	3.83	No	-	-	-	-	-	-	-	-	-	-
396	QP	LTε	4.17	19.78	3.91	No	-	-	-	-	-	-	-	-	-	-
467	SL	LTε	4.61	142.31	7.42	No	-	-	-	-	-	-	-	-	-	-
492	SL	LTε	3.89	21.51	3.69	No	-	-	-	-	-	-	-	-	-	-
500	SL	4.46	4.18	33.06	4.12	No	-	-	-	-	-	-	-	-	-	-
502	SL	4.43	4.17	39.18	4.26	No	137.55	10.80	124.87	7.03	No	-	-	-	-	-
506	SL	5.51	4.58	101.54	6.11	No	-	-	-	-		-	-	-	-	-
507	SL	LTε	4.07	44.53	4.13	No	37.35	5.79	30.23	3.69	No	-	-	-	-	-
528	CS	9.92	6.09	186.47	9.30	Yes (Mild)	-	-	-	-	-	-	-	-	-	-
578	CS	LTε	4.87	300.26	10.58	No	-	-	-	-	-	-	-	-	-	-
581	CS	5.51	4.78	95.62	6.29		8.87	5.67	105.84	7.32	No	-	-	-	-	-
606	CS	9.59	6.08	346.99	11.97	No	9.57	6.08	346.99	11.97	No	-	-	-	-	-
652	MB	LTε	4.28	11.22	3.07	Yes (Mild)	21.70	5.27	75.15	5.73	No	-	-	-	-	-
714	DO	LTε	10.19	1853.86	29.39	No	7.49	6.47	817.54	16.19	No	-	-	-	-	-
760	CS	LTε	4.85	174.98	7.25	No	-	-	-	-	-	LTε	4.98	168.24	7.81	Yes
809	MB	7.08	5.16	34.53	4.46	Yes	-	-	-	-	-	6.94	4.92	27.38	4.69	Yes

E297

Table 10: Result of XRF measurement of samples from CHUE 297. High values of gold in green. **LTε** = values below the device measured error

CHUE-297	Lithology	Matrix Au	Au error	As	As error	Acid	Vein Au	Au error	As	As error	Acid
57	SM	5.21	5.06	5.24	3.01	Yes	5.71	5.03	6.10	3.04	Yes
103	CS	LTε	5.01	58.28	5.08	Yes	5.56	5.14	114.99	6.88	Yes
153	SM	LTε	4.92	2.63	2.92	Yes	6.23	5.08	19.73	3.85	Yes
203	SM	6.11	5.18	2.59	3.04	Yes	-	-	-	-	-
248	SM	5.38	5.14	92.52	6.44	Yes	LTε	4.96	70.01	5.78	Yes
307	SM	LTε	5.09	4.21	3.14	Yes	5.87	5.30	1.35	2.88	Yes
357	QP	LTε	4.14	3.47	3.28	No	-	-	-	-	-
404	QP	LTε	4.26	29.21	4.55	No	-	-	-	-	-
458	QP	LTε	4.08	1.44	3.38	No	-	-	-	-	-
503	QP	LTε	3.98	3.98	3.51	No	-	-	-	-	-
551	QP	LTε	4.05	19.62	4.04	No	-	-	-	-	-
601	QP	LTε	4.08	43.13	5.16	No	-	-	-	-	-
658	QP	LTε	4.15	6.81	3.85	No	-	-	-	-	-
702	QP	LTε	4.06	12.65	3.68	No	-	-	-	-	-
752	MI	6.87	5.20	113.90	6.74	Yes	5.20	4.66	35.91	4.41	Yes
796	MI	22.40	5.92	111.31	6.48	No	-	-	-	-	-
858	QP	LTε	4.25	50.54	5.60	No	-	-	-	-	-
902	MI	LTε	4.08	31.32	3.90	Yes	-	-	-	-	-
949	QP	LTε	37.65	29.80	62.50	No	-	-	-	-	-
1007	QP	LTε	4.00	17.49	3.51	No	-	-	-	-	-
1052	MI	5.62	4.99	8.43	3.24	Yes	LTε	4.74	4.08	2.87	Yes
1104	QP	LTε	4.13	12.69	3.58	No	-	-	-	-	-
1152	CS	5.20	5.01	23.48	4.04	Yes	6.81	5.07	15.19	3.69	Yes
1198	DO	LTε	4.26	4.92	2.59	Yes (Mild)	-	-	-	-	-

E352

Table 11: Result of XRF measurement of samples from CHUE 352. High values of gold in green. **LTε** = values below the device measured error

CHUE-352	Lithology	Matrix					Vein					breccia/clasts				
		Au	Au err	As	As err	Acid	Au	Au err	As	As err	Acid	Au	Au err	As	As error	Acid
51	MI	5.97	5.03	6.53	3.27	Yes	7.06	5.17	3.01	2.97	Yes	6.68	5.00	4.21	3.02	Yes
97	CS	LTε	14.06	8.68	13.30	Yes	-	-	-	-	-	LTε	4.95	307.29	10.46	Yes
152	QP	LTε	5.20	42.65	5.16	-	-	-	-	-	-	-	-	-	-	-
203	MB	5.94	5.35	28.90	4.50	Yes	6.10	5.35	28.12	4.52	Yes	-	-	-	-	-
252	MI	6.62	5.33	8.55	3.37	Yes	5.64	5.14	52.70	4.72	Yes	-	-	-	-	-
305	QP	LTε	4.07	1.93	3.10	No	-	-	-	-	-	-	-	-	-	-
350	QP	LTε	4.02	2.91	3.03	No	-	-	-	-	-	-	-	-	-	-
405	SM	5.46	5.14	88.67	6.32	Yes	5.54	5.09	74.67	5.85	Yes	7.80	5.33	156.44	7.63	-
448	QP	LTε	4.06	53.21	5.17	No	-	-	-	-	-	-	-	-	-	-
500	CS	LTε	4.85	274.73	10.00	No	-	-	-	-	-	-	-	-	-	-
554	SM	11.60	6.12	61.44	5.44	Yes	-	-	-	-	-	-	-	-	-	-
600	MI	19.11	5.27	64.35	5.21	No	13.27	6.45	487.61	13.85	No	-	-	-	-	-
650	MI	LTε	4.41	99.53	6.13	No	-	-	-	-	-	-	-	-	-	-
708	DO	5.25	4.87	68.80	5.41	Yes(Mild)	-	-	-	-	-	-	-	-	-	-
798	DO	LTε	4.66	49.98	4.78	Yes(Mild)	LTε	4.82	168.50	7.80	Yes(Mild)	-	-	-	-	-
851	CS	LTε	4.42	62.21	5.05	Yes(Mild)	5.24	4.84	56.50	5.09	No	-	-	-	-	-
901	CS	6.68	4.99	91.13	6.03	Yes(Mild)	7.29	5.15	145.20	7.22	Yes(Mild)	-	-	-	-	-
946	CS	LTε	4.63	22.77	3.75	Yes	LTε	4.72	81.32	5.95	Yes	-	-	-	-	-
992	CS	LTε	4.52	43.38	4.35	Yes	LTε	4.34	8.63	3.08	Yes	-	-	-	-	-
1050	CS	LTε	4.66	28.65	4.12	Yes	LTε	4.98	152.23	6.88	Yes(Mild)	-	-	-		-
1205	CS	LTε	5.02	4.47	3.04	Yes	5.72	5.22	2.24	2.97	Yes	-	-	-		-

5.   DISCUSSION

In this chapter, the results of the sample investigation, mineral identification and mapping as well as the results of the XRF analyses and their implication are discussed. Sections covered include the differences in the mineralogy and lithology of the sample, the differences between the RGB and SWIR images used for mineral mapping; highlighting their strength and weaknesses. And finally, the collaboration of the XRF results with the mineral maps to determine the textures that may indicate the occurrence of gold within the dataset.

5.1.   Lithological and mineralogical differences

The drill core samples can be broadly classified into siliclastic carbonates and porphyrytic igneous rock . The mineral maps created show silty limestone and micrite having matrixes which were mostly featureless in the SWIR except for a shallow absorption at 2290nm. This carbonate feature was indicated the presence of carbonates in the matrix and was confirmed using an acid. These samples also contained white veins which were identified to be calcite. Some silty limestone samples containing calcite veins were surrounded by a layer of low reflectance grey mineral. These veins could be indicators of the mid to late stage carbonization that occurs during the silicification process common to the study area.
Silty limestone and micrite samples near contact with the porphyries had porhyroblastic textures. They contained grey lens-like rectangular clasts of white micas and montmorillonite.

Mineral maps of calcareous siltstone samples in CHUE-264, show that the samples did not possess any pure carbonate mineral, having been mixed with or replaced prior by white mica minerals and kaolinite. This same type of replacement of carbonates by clays can also be observed in dolostone samples. In dolostone sample "E264_714m", the carbonate minerals in the sample have been completely replaced by kaolinite and illite. These are indicative of decarbonization, and silicification saw in the dissolution of the origin carbonate mineral and replacement by the phyllosilicate minerals. Sample e352_1050m has the mixed class 2, has the same feature as tremolite and Mg-chlorite, and al-oh feature near 2210nm. And a deeper feature at 2380nm. Sample E264_652 contains of the vein of mixed class 3 is which a mixture of clay and carbonate mineral with spectral features in 2202nm and 2292nm features.

Porphyry was mostly classified as white micas or kaolinite. This is also indicative of argillic alteration common to the study area (Li & Peters, 1998). Samples of feldspar porphyries had been altered into white micas. There were variations in the wavelength position of the deepest absorption features of the white micas. Shorter wavelength white micas are richer in aluminium while longer wavelengths are richer in silica (Si) and or magnesium (Mg) and iron cations (Fe) ((Swayze et al., 2014)s). The longer wavelength phengitic muscovite vein in the porphyry has a high Au grade of 14.93ppm. Felsic plutons and dikes have been noted to be mineralized in some deposits (Bergen et al., 2012) Porphyry sample e297_357m and_1104m contained small lenses of calcite.

Some samples of the Porphyry contained striping and can be observed in the distribution of the white mica classes. This is most likely influenced by the initial stripping error in the SWIR images. Though this was corrected, the correction did not totally eliminate the influence of this striping on the position of the absorption minimal of the deepest features around the 2208nm feature common to white micas.

Mixed mineral classes 2 and 3 were different mostly because of the variation of in the depth of absorption between carbonate and Al-OH absorption features in the mix. The more prominent absorption determined the class the mixture was classified as. Sample E352_901m was predominantly a mixture with higher concentrations of carbonates containing veins with higher concentrations of clays.

5.2.   Comparison of the two types of images

The two types of images perform well when highlighting mineral clusters of contrasting colours with the surrounding matrix, for example, white veins in dark matrix. The SWIR images performed best in differentiating between mineral classes because identification was based on the variation in their absorption features of these minerals. Even similar mineral groups with slight variations white micas or the various carbonate mineral were highlighted. This also allowed the identification of longer wavelength phengitic micas bearing higher gold concentration which couldn't be mapped in the RGB images.

The RGB photos perform better when there are differences in brightness of the minerals, for example, dark grey minerals and light grey minerals and layering in the matrix of silty limestone and micrite samples. Whereas, the SWIR images couldn't delineate between them because of the similarity in their spectra See Sample E264_322. They also performed well in highlighting reddish oxidization stains, for example, the reddish weathering and layering in sample E264_271 altered veins seen in mineralized Silty Limestone samples were highlighted by the classified RGB images. The classification obtained from the SWIR images didn't highlight this while the RGB's did. Also, thin white veins of calcite and white micas that were surrounded by a dark grey matrix with low reflectance were not classified properly in the SWIR images. The porphyritic textures weren't properly mapped in the DT classification of the RGB images. While the porphyry texture was visible in RGB, their mineralogy was like the surrounding ground mass and therefore not properly delineated. Porphyry samples of E297 contain colourless crystals which were classified as clays & micas and weren't different from the surrounding matrix. The RGB also couldn't differentiate between these minerals.

However, it should be noted that the hue and tone of the minerals could be influenced by illumination conditions during image acquisition. White minerals observed in the RGB were commonly identified to be calcite and white micas in the SWIR while dark grey was commonly identified to be mixed class1. In some cases, light grey minerals were either classified as white micas or mixed class1. Orange minerals were classified as kaolinite while reddish brown minerals were observed in oxidized samples.

5.3.   Textural differences with depth

Samples within the approximate depth of 300m to 600m in all three drill hole show signs of argillic alteration. This alteration was mostly observed within the Porphyry samples. Porphyry samples obtained from depths shallower than this range were mostly classified as illite though they contained phenocrysts of kaolinite. The presence of illite may have been by-product of the weathering of pre-existing feldspars. However, towards 300 to 600m deep, kaolinite concentrations increased and then began to decline beyond this depth range. Calcareous siltstone in this range also exhibit characteristics consist with oxidation. Oxidation can also be seen in silty limestone at this range. The XRF measurement on calcite veins of samples of silty limestone at shallow depth showed with little to no gold and typically having lower concentrations than in their matrix (see sample e264_51 in table 8) this coincides with paragenetic models that show calcite occurring late in the hydrothermal alteration process after gold mineralization (Arehart, Chryssoulis, & Kesler, 1993)

5.4.   Gold mineralization and textures

The XRF measurement was done to investigate the gold concentrations within textures identified from the images. This method was used to collaborate the existing fire assay result, which already identified samples

within the stratigraphic column, which were mineralized. The comparison of these two results helps to identify textures that were indicative of mineralization or otherwise.

5.4.1. Gold content from fire assay auxiliary data

The result of the fire assay (FA) can be seen in tables 4 to 6 above. The measurement interval was 5-10m of cores. With this information, the cut-off grade of 0.15ppm Au for waste and 5.14ppm Au for distinguishing between high- and low-grade ore (Dalm, 2018) was used to identify samples with for the dataset that were mineralized. The mineralized samples identified include; six samples from CHUE-264 were identified to be mineralized samples. These samples are E264_492m (SL_c), 500m(SL_b), 502m (SL_b), 506m (SL_b), 507m (SL_b) and 528m (CS_b). Only two samples from CHUE-297 were identified to be mineralized, they were E297_503m(QP_a), and 796m(MI_a). While for CHUE352, three samples were identified to be mineralized. They were E-352_554m (SM), 600m (MI_b), 650m (MI_b). These samples are displayed in figure 19 below.

The results of the FA show that silty limestone samples from CHUE 264 host the zone of Au mineralization (*see Table 3*). This lithology had samples that were both mineralized and unmineralized. The samples identified as mineralized were those with Au ppm values above 0.15pp, which is the cut-off grade. The result also shows that the zone of highest mineralization was near the porphyry intrusions. Table 4, which shows the result of the fire assay for E264, shows that five of the silty limestone samples had gold above 0.15ppm. These samples were unlayered (SL-b) while the rest of the SL samples which were below 0.15ppm had matrixes showed layering pattern in their matrixes. The intrusive porphyries samples mostly were unmineralized with AU ppm values below 0.15ppm, except for sample E297_503m which had a value of 0.32ppm.

In total 11 samples from the 3 drill holes had ppm Au values above 0.05ppm. The minerals most commonly mapped in these samples were the mixed class1 minerals and white micas and in some cases clays.

The textures that can be observed in these samples include veins of montmorillonite and micas hosted in silty carbonate matrix, two samples fine-grained micritic grey matrix and white micas in weathered porphyry were potential indicators of mineralization in this deposit.
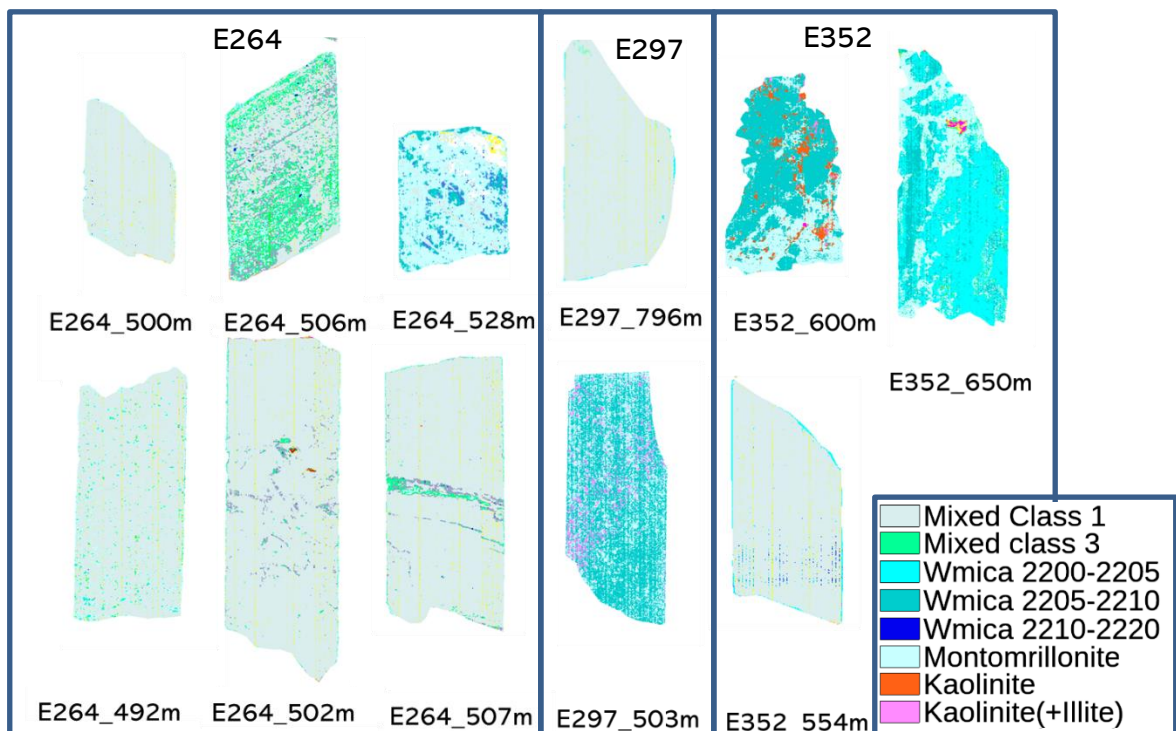
Figure 19: Samples with Au ppm greater than 0.15ppm from fire assay

5.4.2. Gold content from XRF measurement

Different textures were measured using the pXRF device. Some of these textures contained gold but occurred within matrixes without gold or inversely had matrix with gold but contained textures like veins that didn't contain gold. The results show that 8 samples from the three drill holes had Au occurring in concentrations higher than 11ppm.

5.4.2.1. Samples with high concentrations of gold via XRF

The pXRF allowed the identification of mineral clusters containing gold or otherwise. These samples include; E264_271m, E264_300m(SL_b). E264_318m(SL_b), E264_502m(SL_b), E264_507m(SL_b) E297_796m(MI) E352_554m(MI_a) and E352_600m(MI_b) (see Figure 20). However, only five of these samples were part of the eleven identified in from the FA. Though, three new samples that were identified by the XRF measurements; namely e264_271m and E264_303m and E264m_318m. Of these three samples, only samples e264_318m had a value of 0.116ppm from the fire assay close to but below the cut-off grade of 0.15ppm while in the XRF measurement it contained veins of calcite plus dolomite with an approximate value of 11.3ppm. The reason for this disparity is most likely the 5-10m interval of the FA. Dalm 2018 identified dolomite to be associated with ore samples.

A phengitic white mica vein was identified in sample E264_271m with a value of 14.93ppm Au; while veins of white mica mixed with carbonate (mixed class 3) in SL samples E264_507 contained 37.4ppm Au and red oxidized clay veins in sample E264_502 had a value of 137 ppm Au.

The results show that white micas veins within carbonate matrix of micrite and dark grey silty limestone or silty micrite had high gold contents above 11ppm. Also, oxidized veins in this category have the highest concentrations of gold which was probably caused by supergene enrichment that occurred post mineralization.
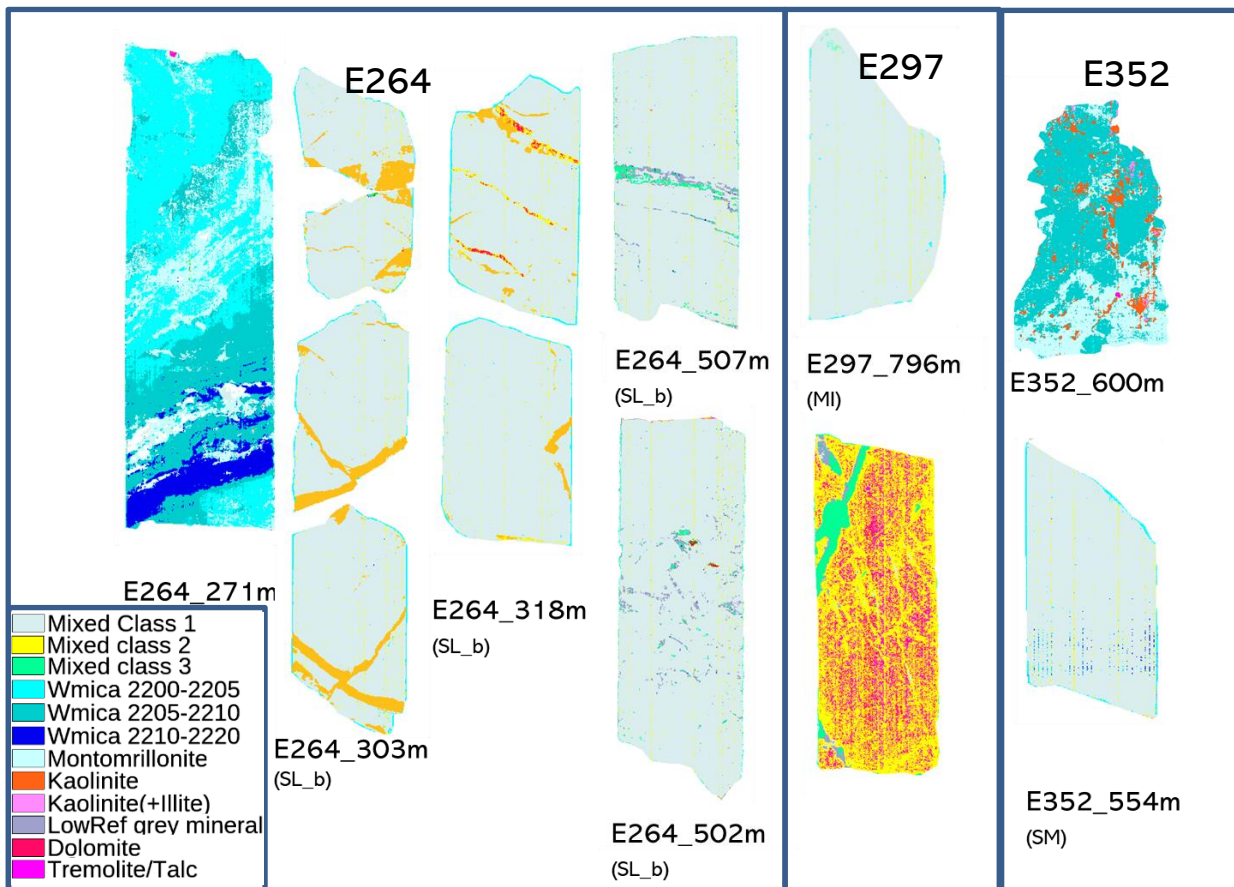
Figure 20 : Samples with high concentrations of Au (above 11ppm) from XRF measurement.

5.4.2.2. Samples potentially containing low concentrations of gold

Some other samples showed indications of mineralization and might require further investigation using a method with a lower detection limit. 'Indication of mineralization' is a term used in this study for samples whose pXRF measurement results have considerable concentrations of gold and arsenic which occurs together with Au in the study are and whose measured Au response were actual values and these values were higher than the measured error. Typically, when the device cannot measure a given element, the device returns a value of 'LOD'.

The samples that fall into this category are displayed in Figure 21. Consequently, it can be observed that the altered calcareous samples. E264_528m,581m and 606m, had values that showed indications of gold in their clayey and micaceous matrix or veins. Also, layered silty limestone matrixes had this indication while their calcite veins did not. An example is the vein in sample e264_51m though calcite veins in layered matrix samples like E264_303m and 318m had indications of gold. Though sample e264_51m did not contain gold in its vein, its matrix showed indications of mineralization. It should be noted that while the samples show signs indicative of the presences of gold, this doesn't mean gold occurs in concentrations of economic proportions.

Samples of dolostone and calcareous siltstone which hadn't be replaced by clays and micas didn't contain gold. Layered matrixes silty carbonates like silty limestone and silty micrite which contained carbonates had indications of the presence of gold within their matrixes while unlayered dark grey matrixes without carbonates were unmineralized.
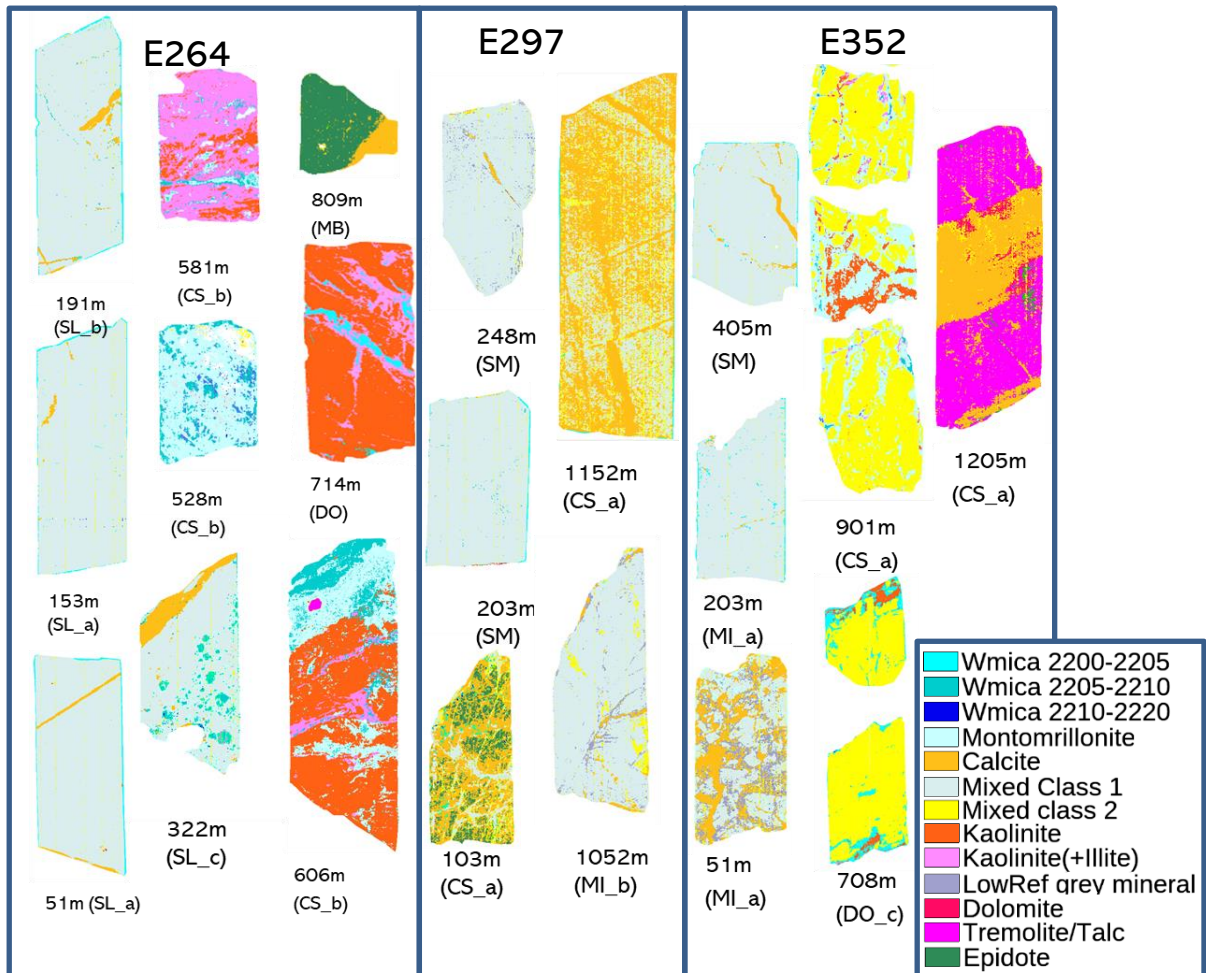
Figure 21 : Samples with indications of Au from XRF. The XRF measurement response is higher that the error measurement.

5.5. XRF measurement uncertainty

The effective range of an XRF measurement as well as its limit of detection is dependent on a tube and detector of the portable XRF, and the matrix of the sample investigated, for instance, the present of heavier major elements like iron negatively impact the detection of trace elements (Lemière, 2018).

The mode of the measurements of the samples was by spot measurement on the different textures identified such as matrix, veins and breccias/clast. The values of Au typically had an error margin of $\pm$ 4ppm to $\pm$6ppm. All these might have contributed to the anomalously high values observed in the XRF results (see Appendix 3 4 and 5). Though these measurements were below the reliable detection limit set by the manufacturer (11ppm for Au) the device still recorded responses from samples with concentrations below this value. Many of the samples had abnormally high values of A, which were unexpected, considering the results of the Fire assay (very low to near 0 values). Therefore, should these samples contain Au, they should not have values as high as 5ppm and above. One possible reason for these anomalous values could be the influence of background. Another source of uncertainty is the true representability of the spot measurement used to carry out the XRF analysis. A whiskey plot of some measurements showed a high variability in the values of repeat measurements. From the whisker plot displayed in Figure 22, there is a high variance in the measurements of Au while the variance was low for the measurement error .
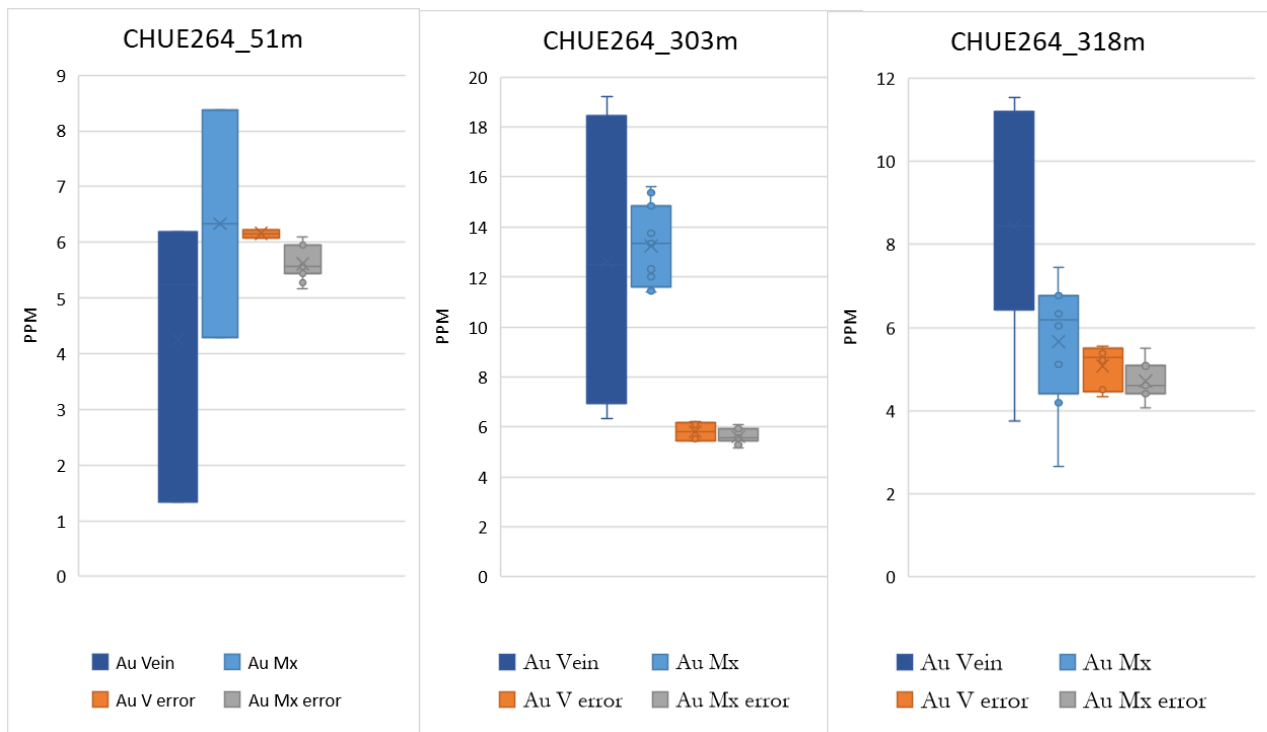
Figure 22: Plot showing range of values of gold concentration in vein and matrix with the error of XRF measurement in for sample E264_51m, E264_303 AND E264_318m

6. CONCLUSION AND RECOMMENDATIONS

6.1. Conclusion

Hyperspectral shortwave infrared images were useful in identifying both the mineralogy and highlighting textures from samples of ores. This is informative because mapping minerals alone without taking in textural information into consideration may not yield an accurate understanding of the mineralization in the study area. This research was able to map minerals and categorize the textures observed in samples of carlin-type gold deposits acquired by the Barrick Gold Corporation using hyperspectral shortwave infrared images (SWIR) and Red Green and Blue (RGB) photo.

The two types of images used in the research performed well in highlighting textures from the samples. The RGB images were classified based on the colour ratio of the red, green and blue bands (RGB) and were able to highlight textures though they couldn't clearly differentiate between minerals classes particularly when they were of the same colour. Meanwhile, the SWIR images were able to differentiate between even white micas with varying aluminium concentrations.

X-ray fluorescence analysis using a portable XRF (pXRF) was used to carry out spot measurements on the drill core samples to obtain the concentration of the elements in them, particularly gold. Two elements of interest were gold and arsenic. Measurement was carried out on identified textures such as the different matrixed, veins and clasts. The collaboration of the mineral maps, the fire assay and XRF result show the zone of most mineralization was in the silty limestones of drill hole CHUE-264 which had been intruded by the Porphyries. It also showed that white mica veins in dark grey silty carbonate and white mica mixed with carbonate (mixed class 3) non- carbonate matrixes contained high gold concentrations; above 11ppm. Also, a phengitic mica vein was found in weathered porphyry containing high gold concentration. While silty carbonate matrixes of silty limestone and micrite showed indication of gold mineralization but had values that were below the detection limit of the pXRF. Most calcite veins were unmineralized though some calcite veins at depths show indication of gold mineralization. This why the inability to differentiate between mineral is a short coming of the RGB images because it is important to be able to discriminate between white micas veins and those of calcites when they occurred in dark grey silty matrixes. The former (white micas) contains Au, sometimes in high concentrations while the latter (calcite veins) contained little to no gold. Other textures with gold or indications of gold include silty carbonate matrixes like the silty limestone and the silty micrite and montmorillonite veins in carbonate matrix. Most porphyry samples didn't contain gold, except for samples that had been weathered. Supergene enrichment of clay and mica veins show a high concentration of gold. This alteration occurred after mineralization in the study area. Argillic alteration was also observed in samples approximately between 300m to 600, which collaborates the existing study that shows the study area has undergone alteration.

6.2. Recommendation

Samples suspected to contain gold should be further investigated using a method with higher precision. Further work should be carried out on the textures identified in this research to extract their parameters. These parameters can be used to create a quantitative new model which, like Goetz et al., (2009) research's, can be transferred to mining installations to enhance ore sorting. This would improve ore sorting, lead to better optimisation of the mineral liberation process and would reduce operation cost for industries (Goetz et al., 2009).

The limitation of the XRF measurement can also be improved by using a Laboratory XRF analyser like the WDXRF. The mapping mode of this device can be used to measure element concentrations across the surface of entire samples instead of relying on spot measurements which may not be representative of the entire surface of the sample.

LIST OF REFERENCES

Anthony, J. W., Bideaux, R. A., Bladh, K. W., & Nichols, M. C. (Eds.). (2010). Tremolite. In *Handbook of Mineralogy* (Vol. 2, pp. 1425–1425). Chantilly, VA 20151-1110, USA.: Mineralogical Society of America. https://doi.org/10.1007/978-3-642-41714-6_202550

Arehart, G. B., Chryssoulis, S. L., & Kesler, S. E. (1993). Gold and arsenic in iron sulfides from sediment-hosted disseminated gold deposits: Implications for depositional processes. *Economic Geology*, *88*, 171–185. https://doi.org/10.2307/25007866

Asadzadeh, S., & de Souza Filho, C. R. (2016). A review on spectral processing methods for geological remote sensing. *International Journal of Applied Earth Observation and Geoinformation*, *47*, 69–90. https://doi.org/10.1016/J.JAG.2015.12.004

Bakker, W. H. (2012). HypPy User Manual. *ITC - University of Twente*. Retrieved from http://www.itc.nl/personal/bakker/hyppy.html

Barton, P. B. (1991). Ore Textures: Problems and Opportunities. *Mineralogical Magazine*, *55*(380), 303–315. https://doi.org/10.1180/minmag.1991.055.380.02

Bergen, R. D., Gareau, M. B., Altman, K. A., & Clow, G. (2012). Technical report on the Cortez Joint Venture Operations, Lander and Eureka Counties, State of Nevada, U.S.A. Toronto, Ontario: Roscoe Postle Associates Inc.

Bevan, M. J. D. (2018). High-resolution Short-wave Infrared (SWIR) hyperspectral characterisation of alteration at the Cortez Hills Carlin-Type Gold (Unpublished Msc Thesis).

Britannica.com. (2011). Matrix | geology | Britannica.com. Retrieved May 16, 2019, from https://www.britannica.com/science/matrix-geology

Clark, L. R. (2012). *Ore and Gangue Mineral Paragenesis of the Cortez Hills Carlin-Type Gold Deposit , Nevada : Evidence for Coincident High-Grade Gold Deposition and Collapse Brecciation (Unpublished Msc Thesis)*. University of Nevada, Las Vegas.

Colgan, J. P., Henry, C. D., & John, D. A. (2008). Geologic map and cross sections of the Caetano Caldera, Lander County, Nevada. *Geosphere*, *Volume 4*(1). https://doi.org/10.1130/GES00115.1.Deino

Craig, J. R., & Vaughan, D. (2005). Ore Mineral Textures. In *Ore microscopy*. (pp. 120–163).

Dalm, M. (2017). *XRD identification of pulverized rock samples*. Delft.

Dalm, M. (2018). *Sensor-based sorting opportunities for hydrothermal ore deposits: Raw material beneficiation in mining*. Technische Universiteit Delft. https://doi.org/10.4233/uuid:70a1e180-ef0c-4226-9af3-7e9dc3938c7f

Dalm, M., Buxton, M. W. N., van Ruitenbeek, F. J. A., & Voncken, J. H. L. (2014). Application of near-infrared spectroscopy to sensor based sorting of a porphyry copper ore. *Minerals Engineering*, *58*, 7–16. https://doi.org/10.1016/j.mineng.2013.12.016

Environmental Protection Agency. (2016). *Definition and Procedure for the Determination of the Method Detection Limit , Revision 2*.

Garwin, S. (2005). Geologic Overview of the Gold Deposits of the, *6907*.

Gay, S. L. (2004). Simple texture-based liberation modelling of ores. *Minerals Engineering*, *17*(11–12), 1209–1216. https://doi.org/10.1016/J.MINENG.2004.06.032

Gilluly, J., & Masursky, H. (1965). Geological Map and Sections of the Cortez Quadrangle, Nevada.pdf. Washington. D.C., USA: Geological Survey.

Goetz, A. F. H., Curtiss, B., & Shiley, D. A. (2009). Rapid gangue mineral concentration measurement over conveyors by NIR reflectance spectroscopy. *Minerals Engineering*, *22*(5), 490–499. https://doi.org/10.1016/J.MINENG.2008.12.013

Govil, H. (2015). Prospecting for hydrothermal mineral deposits in the Himalaya using short-wave infrared spectroscopy. *2015 7th Workshop on Hyperspectral Image and Signal Processing: Evolution in Remote Sensing (WHISPERS)*, 1–4. https://doi.org/10.1109/WHISPERS.2015.8075363

Guiral-Vega, J. S. (2018). Textural and Mineralogical Characterization of Li-pegmatite Deposit : Using Microanalytical and Image Analysis to Link Micro and Macro Properties of Spodumene in Drill Cores (Unpublished Msc Thesis).

Higgins, M. D. (2006). *Quantitative textural measurements in igneous and metamorphic petrology. Quantitative Textural Measurements in Igneous and Metamorphic Petrology*. https://doi.org/10.1017/CBO9780511535574

Hilden, M. M., & Powell, M. S. (2017). A geometrical texture model for multi-mineral liberation

prediction. *Minerals Engineering*, *111*, 25–35. https://doi.org/10.1016/J.MINENG.2017.04.020

Hofstra, A., & Cline, J. (2000). Characteristics and models for Carlin-type gold deposits. *Reviews in Economic Geology*, *13*(July), 163–220. Retrieved from https://www.researchgate.net/publication/304335923

Homayouni, S., & Roux, M. (2014). Hyperspectral image analysis for material mapping using spectral matching HYPERSPECTRAL IMAGE ANALYSIS FOR MATERIAL MAPPING, (May 2014).

Iyakwari, S., Glass, H. J., & Obrike, S. E. (2017). Discerning mineral association in the near infrared region for ore sorting. *International Journal of Mineral Processing*, *166*, 24–28. https://doi.org/10.1016/j.minpro.2017.06.008

Kamruzzaman, M., & Sun, D. W. (2016). Introduction to Hyperspectral Imaging Technology. In *Computer Vision Technology for Food Quality Evaluation: Second Edition* (pp. 111–139). Elsevier Inc. https://doi.org/10.1016/B978-0-12-802232-0.00005-0

Lemière, B. (2018). A review of pXRF (field portable X-ray fluorescence) applications for applied geochemistry. *Journal of Geochemical Exploration*, *188*(February), 350–363. https://doi.org/10.1016/j.gexplo.2018.02.006

Li, Z. P., & Peters, S. G. (1998). Comparative geology and geochemistry of sedimentary- Republic of China and in Nevada , USA., 1–160. https://doi.org/10.3133/ofr98466

mindat.org. (2019). Silt: Mineral information, data and localities. Retrieved May 9, 2019, from https://www.mindat.org/min-49428.html

Misture, S. T., & Snyder, R. L. (2001). X-ray Diffraction. In *Encyclopedia of Materials: Science and Technology* (pp. 9799–9808). Elsevier Ltd.

Pérez-barnuevo, L., Lévesque, S., & Bazin, C. (2018). Drill core texture as geometallurgical indicator for the Mont-Wright iron ore deposit (Québec , Canada) Drill core texture as geometallurgical indicator for the Mont-Wright iron ore deposit (Quebec , Canada). *Minerals Engineering*, *122*(April), 130–141. https://doi.org/10.1016/j.mineng.2018.03.020

Pontual, S., Merrry, N.,& Gamson, .P. (1997). G-Mex Spectral Interpretation Field Manual. Ausspec Internatoonal.

Roger N. Clark. (1999). Spectroscopy of Rocks and Minerals and Principles of Spectroscopy. Manual of Remote Sensing. In *Remote Sensing for the Earth Sciences* (Vol. 3, pp. 3–58). Denver, Colorado: U.S. Geological Survey.

Savan Patel. (2017). Chapter 3 : Decision Tree Classifier — Theory – Machine Learning 101 – Medium. Retrieved August 27, 2018, from https://medium.com/machine-learning-101/chapter-3-decision-trees-theory-e7398adac567

Scott, K. M., & Yang, K. (1997). Spectral reflectamce study of white micas. Melbourne, Australia: Australian Mineral Industries Research Association Limited.

SPECIM. (2015). SisuCHEMA: spectral camera. Oulu, Finland: Spectral Imaging Ltd.

Swayze, G. A., Clark, R. N., Goetz, A. F. H., Livo, K. E., Breit, G. N., Kruse, F. A., … Ashley, R. P. (2014). Mapping advanced argillic alteration at Cuprite, Nevada, using imaging spectroscopy. *Economic Geology*, *109*(5), 1179–1221. https://doi.org/10.2113/econgeo.109.5.1179

Thermo Scientific. (2010). Thermo Scientific Niton XL3t GOLDD + Series Mining Analyzers, 3.

Thermo Scientific. (2012). Application of the Thermo Scientific Portable XRF Analyzer in PGE Exploration. Munich, Germany: Thermo Fisher Scientific.

Turner, D., Groat, L. A., Rivard, B., & Belley, P. M. (2017). Reflectance spectroscopy and hyperspectral imaging of sapphire-bearing marble from the Beluga Occurrence, Baffin Island, Nunavut. *The Canadian Mineralogist*, *55*(4), 787–797. https://doi.org/10.3749/canmin.1700023

USGS. (n.d.). Cortez Hills (Sed-Au #55) deposit in Nevada, U.S.A. Retrieved August 29, 2018, from https://mrdata.usgs.gov/sedau/show-sedau.php?recno=55

van der Meer, F. (2004). Analysis of spectral absorption features in hyperspectral imagery. *International Journal of Applied Earth Observation and Geoinformation*, *5*(1), 55–68. https://doi.org/10.1016/j.jag.2003.09.001

van der Meer, F. (2018). Near-infrared laboratory spectroscopy of mineral chemistry: A review. *International Journal of Applied Earth Observation and Geoinformation*. Elsevier. https://doi.org/10.1016/j.jag.2017.10.004

van Ruitenbeek, F. J. A., Bakker, W. H., van der Werff, H. M. A., Zegers, T. E., Oosthoek, J. H. P., Omer, Z. A., … van der Meer, F. D. (2014). Mapping the wavelength position of deepest absorption features to explore mineral diversity in hyperspectral images. *Planetary and Space Science*, *101*, 108–117. https://doi.org/10.1016/J.PSS.2014.06.009

Van Ruitenbeek, F. J. A., Debba, P., Van Der Meer, F. D., Cudahy, T., Van Der Meijde, M., & Hale, M.

(2006). Mapping white micas and their absorption wavelengths using hyperspectral band ratios, *102*, 211–222. https://doi.org/10.1016/j.rse.2006.02.012

Viktor Gavrilov. (2016). Benefits of decision trees in solving predictive analytics problems | Prognoz blog. Retrieved August 29, 2018, from http://www.prognoz.com/blog/platform/benefits-of-decision-trees-in-solving-predictive-analytics-problems/

Webmineral.com. (2012). Tremolite Mineral Data. Retrieved May 11, 2019, from http://www.webmineral.com/data/Tremolite.shtml#.XNchC-gzaUl

Wilson, D. J., Christiansen, E. H., & Tingey, D. G. (1994). Geology and Geochemistry of the Golden Butte Mine -- A Small Carlin-Type Gold Deposit in Eastern Nevada. *BYU Geology Studies*, *40*.

Zhu, Y., An, F., & Tan, J. (2011). Geochemistry of hydrothermal gold deposits : A review. *Geoscience Frontiers*, *2*(3), 367–374. https://doi.org/10.1016/j.gsf.2011.05.006

APPENDIX

Appendix 1: Decision tree classifier of RGB images. b1 = blue, b2 = green, b3 = red
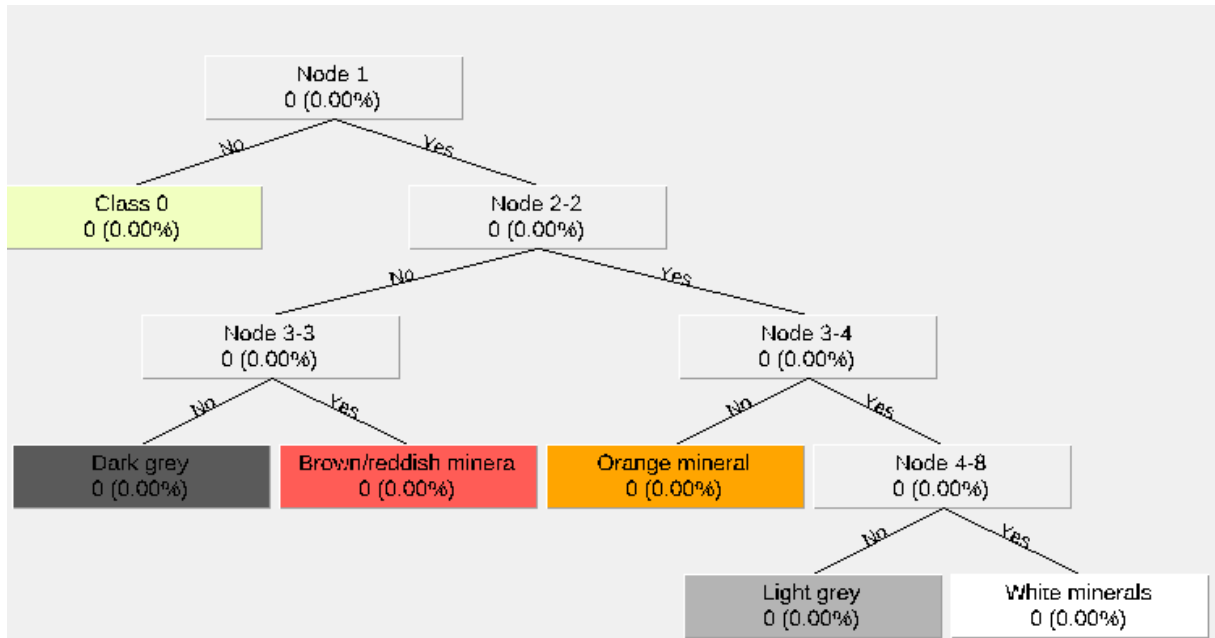
Appendix 2: Result of XRF measurement of samples from CHUE 264

CHUE-264	Lithology	Matrix								Vein								breccia/clasts							
		Au	Au error	As	As error	Fe	Ca	Si	Acid	Au	Au err	As	As err	Fe	Ca	Si	Acid	Au	Au error	As	As error	Fe	Ca	Si	Acid
51	SL	6.33	5.42	3.18	3.16	0.23%	39.45%	5.87%	Yes	4.25	4.94	2.91	3.27	0.22%	33.44%	10.93%	Yes	-	-	-	-	-	-	-	-
102	SL	5.19	5.09	2.03	3.21	0.19%	38.65%	5.71%	Yes	-	-	-	-	-	-	-	Yes	-	-	-	-	-	-	-	-
153	SL	6.77	5.29	5.98	3.13	0.13%	43.59%	3.01%	Yes	7.83	5.46	10.22	3.43	0.12%	44.98%	2.05%	Yes	-	-	-	-	-	-	-	-
191	SL	4.22	4.97	14.87	3.62	0.29%	31.34%	11.41%	Yes	6.12	5.69	24.90	4.30	0.15%	42.99%	2.90%	Yes		-	-	-	-	-		
256	FP	0.83	4.19	3.35	3.51	0.85%	0.59%	30.00%	No	-	-	-	-	-	-	-	-	-	-	-	-	-	-	-	-
264	SL	2.10	4.29	16.98	4.42	0.66%	0.44%	27.48%	No	-	-	-	-	-	-	-	-	-	-	-	-	-	-	-	-
271	FP	2.88	4.67	217.70	8.58	1.54%	0.29%	39.63%	No	14.93	5.84	352.98	11.31	1.52%	0.42%	34.49%	-	-	-	-	-	-	-	-	-
303	SL	13.24	5.62	109.11	6.77	0.57%	26.19%	14.03%	Yes	12.63	5.81	64.19	5.47	0.26%	36.14%	7.42%	Yes		-	-					-
318	SL	6.38	5.23	66.89	5.76	0.39%	37.50%	4.67%	Yes	11.30	5.52	20.20	3.90	0.13%	44.01%	1.25%	Yes	-	-	-	-	-	-	-	-
318b		5.01	4.45	75.61	5.41	0.45%	11.39%	26.24%	Yes	6.99	4.86	51.57	4.84	0.35%	17.44%	20.69%	Yes								
322	SL	8.37	5.28	127.51	7.24	0.39%	28.68%	16.17%	Yes	6.14	5.11	29.95	4.32	0.26%	44.64%	3.03%	Yes	4.38	4.89	83.62	6.53	0.42%	16.60%	21.66%	Yes
352	QP	2.33	4.14	7.96	3.62	0.60%	0.36%	30.58%	No	-	-	-	-	-	-	-	-	-	-	-	-	-	-	-	-
380	QP	0.87	4.07	13.78	3.83	0.56%	0.26%	32.53%	No	-	-	-	-	-	-	-	-	-	-	-	-	-	-	-	-
396	QP	2.92	4.17	19.78	3.91	0.53%	0.22%	33.97%	No	-	-	-	-	-	-	-	-	-	-	-	-	-	-	-	-
467	SL	4.75	4.61	142.31	7.42	1.76%	0.22%	36.83%	No	-	-	-	-	-	-	-	-	-	-	-	-	-	-	-	-
492	SL	0.64	3.89	21.51	3.69	0.24%	0.17%	40.02%	No	-	-	-	-	-	-	-	-	-	-	-	-	-	-	-	-
500	SL	4.46	4.18	33.06	4.12	0.20%	0.13%	42.44%	No	-	-	-	-	-	-	-	-	-	-	-	-	-	-	-	-
502	SL	4.43	4.17	39.18	4.26	0.13%	0.10%	41.47%	No	137.55	10.80	124.87	7.03	2.49%	0.12%	40.09%	No	-	-	-	-	-	-	-	-
506	SL	5.51	4.58	101.54	6.11	1.03%	0.23%	34.78%	No	-	-	-	-	-	-	-		-	-	-	-	-	-	-	-
507	SL	3.36	4.07	44.53	4.13	0.11%	0.20%	41.00%	No	37.35	5.79	30.23	3.69	0.07%	0.20%	41.99%	No	-	-	-	-	-	-	-	-
528	CS	9.92	6.09	186.47	9.30	4.08%	0.28%	29.89%	Yes (Mi	-	-	-	-	-	-	-	-	-	-	-	-	-	-	-	-
578	CS	2.65	4.87	300.26	10.58	1.55%	0.54%	35.51%	No	-	-	-	-	-	-	-	-	-	-	-	-	-	-	-	-
581	CS	5.51	4.78	95.62	6.29	0.85%	5.07%	25.83%		8.87	5.67	105.84	7.32	1.09%	16.41%	16.31%	No	-	-	-	-	-	-	-	-
606	CS	9.59	6.08	346.99	11.97	2.87%	6.27%	25.87%	No	9.57	6.08	346.99	11.97	2.07%	11.99%	23.04%	No	-	-	-	-	-	-	-	-
652	MB	3.83	4.28	11.22	3.07	0.07%	23.85%	4.42%	Yes (Mi	21.70	5.27	75.15	5.73	0.40%	1.22%	44.51%	No	-	-	-	-	-	-	-	-
714	DO	1.83	10.19	1853.86	29.39	7.79%	0.73%	24.47%	No	7.49	6.47	817.54	16.19	4.36%	0.61%	25.70%	No	-	-	-	-	-	-	-	-
760	CS	4.17	4.85	174.98	7.25	1.47%	18.01%	9.71%	No	-	-	-	-	-	-	-	-	4.55	4.98	168.24	7.81	1.13%	16.61%	10.36%	Yes
809	MB	7.08	5.16	34.53	4.46	0.32%	37.30%	4.50%	Yes	-	-	-	-	-	-	-	-	6.94	4.92	27.38	4.69	0.34%	35.16%	5.40%	Yes

Appendix 3: Result of XRF measurement of samples from CHUE 297

CHUE-297	Lithology	Matrix Au	Au err	As	As err	Fe	Ca	Si	Acid	Vein Au	Au err	As	As err	Fe	Ca	Si	Acid	breccia -
57	SM	5.21	5.06	5.24	3.01	0.41%	33.76%	6.25%	Yes	5.71	5.03	6.10	3.04	0.30%	37.60%	4.29%	Yes	-
103	CS	4.91	5.01	58.28	5.08	7.44%	34.42%	7.12%	Yes	5.56	5.14	114.99	6.88	1.93%	29.35%	8.75%	Yes	-
153	SM	3.57	4.92	2.63	2.92	0.51%	35.46%	7.01%	Yes	6.23	5.08	19.73	3.85	0.96%	35.64%	4.06%	Yes	-
203	SM	6.11	5.18	2.59	3.04	0.31%	37.10%	6.07%	Yes	-	-	-	-	-	-	-	-	-
248	SM	5.38	5.14	92.52	6.44	0.26%	31.12%	11.79%	Yes	4.54	4.96	70.01	5.78	0.46%	34.26%	7.74%	Yes	-
307	SM	4.66	5.09	4.21	3.14	0.16%	39.90%	3.33%	Yes	5.87	5.30	1.35	2.88	0.08%	41.17%	1.19%	Yes	-
357	QP	1.64	4.14	3.47	3.28	0.51%	2.38%	32.75%	No	-	-	-	-	-	-	-	-	-
404	QP	2.91	4.26	29.21	4.55	0.65%	0.75%	33.08%	No	-	-	-	-	-	-	-	-	-
458	QP	0.13	4.08	1.44	3.38	0.80%	0.72%	32.24%	No	-	-	-	-	-	-	-	-	-
503	QP	0.15	3.98	3.98	3.51	0.47%	0.86%	32.46%	No	-	-	-	-	-	-	-	-	-
551	QP	1.32	4.05	19.62	4.04	0.56%	0.35%	35.03%	No	-	-	-	-	-	-	-	-	-
601	QP	0.62	4.08	43.13	5.16	0.62%	2.06%	32.73%	No	-	-	-	-	-	-	-	-	-
658	QP	1.53	4.15	6.81	3.85	0.61%	1.63%	32.42%	No	-	-	-	-	-	-	-	-	-
702	QP	1.24	4.06	12.65	3.68	0.13%	2.06%	32.74%	No	-	-	-	-	-	-	-	-	-
752	MI	6.87	5.20	113.90	6.74	0.26%	28.73%	14.26%	Yes	5.20	4.66	35.91	4.41	0.16%	23.72%	15.73%	Yes	-
796	MI	22.40	5.92	111.31	6.48	0.23%	0.31%	34.41%	No	-	-	-	-	-	-	-	-	-
858	QP	1.51	4.25	50.54	5.60	0.53%	0.76%	32.15%	No	-	-	-	-	-	-	-	-	-
902	MI	2.78	4.08	31.32	3.90	0.20%	6.88%	28.58%	Yes	-	-	-	-	-	-	-	-	-
949	QP	0.00	37.65	29.80	62.50	76.81%	0.02%	0.10%	No	-	-	-	-	-	-	-	-	-
1007	QP	1.30	4.00	17.49	3.51	0.20%	0.95%	30.82%	No	-	-	-	-	-	-	-	-	-
1052	MI	5.62	4.99	8.43	3.24	0.29%	34.93%	3.92%	Yes	4.85	4.74	4.08	2.87	0.12%	36.04%	3.11%	Yes	-
1104	QP	3.35	4.13	12.69	3.58	0.16%	1.39%	31.38%	No	-	-	-	-	-	-	-	-	-
1152	CS	5.20	5.01	23.48	4.04	0.24%	34.93%	6.97%	Yes	6.81	5.07	15.19	3.69	0.23%	35.26%	7.12%	Yes	-
1198	DO	2.93	4.26	4.92	2.59	0.04%	25.00%	1.61%	Yes (Mild)	-	-	-	-	-	-	-	-	-

Appendix 4: Result of XRF measurement of samples from CHUE 352

CHUE-352	Lithology	Matrix								Vein								breccia/clasts							
		Au	Au err	As	As err	Fe	Ca	Si	Acid	Au	Au err	As	As err	Fe	Ca	Si	Acid	Au	Au error	As	As error	Fe	Ca	Si	Acid
51	MI	5.97	5.03	6.53	3.27	0.50%	37.53%	4.39%	Yes	7.06	5.17	3.01	2.97	0.36%	42.37%	2.66%	Yes	6.68	5.00	4.21	3.02	0.60%	34.32%	6.10%	Yes
97	CS	3.08	14.06	8.68	13.30	26.75%	16.94%	6.33%	Yes	-	-	-	-	-	-	-	-	2.83	4.95	307.29	10.46	1.98%	10.72%	19.08%	Yes
152	QP	3.26	5.20	42.65	5.16	1.89%	29.00%	10.49%	-	-	-	-	-	-	-	-	-	-	-	-	-	-	-	-	-
203	MB	5.94	5.35	28.90	4.50	0.41%	41.60%	4.76%	Yes	6.10	5.35	28.12	4.52	0.26%	42.40%	3.39%	Yes	-	-	-	-	-	-	-	-
252	MI	6.62	5.33	8.55	3.37	0.12%	42.09%	6.03%	Yes	5.64	5.14	52.70	4.72	1.18%	29.32%	13.44%	Yes	-	-	-	-	-	-	-	-
305	QP	1.44	4.07	1.93	3.10	0.64%	0.42%	31.16%	No	-	-	-	-	-	-	-	-	-	-	-	-	-	-	-	-
350	QP	2.11	4.02	2.91	3.03	0.17%	1.11%	30.19%	No	-	-	-	-	-	-	-	-	-	-	-	-	-	-	-	-
405	SM	5.46	5.14	88.67	6.32	0.37%	39.18%	6.61%	Yes	5.54	5.09	74.67	5.85	0.21%	40.93%	5.43%	Yes	7.80	5.33	156.44	7.63	1.26%	25.22%	17.56%	-
448	QP	1.55	4.06	53.21	5.17	0.39%	0.11%	33.65%	No	-	-	-	-	-	-	-	-	-	-	-	-	-	-	-	-
500	CS	2.50	4.85	274.73	10.00	1.93%	0.54%	32.59%	No	-	-	-	-	-	-	-	-	-	-	-	-	-	-	-	-
554	SM	11.60	6.12	61.44	5.44	0.31%	32.62%	11.32%	Yes	-	-	-	-	-	-	-	-	-	-	-	-	-	-	-	-
600	MI	19.11	5.27	64.35	5.21	0.85%	0.41%	35.79%	No	13.27	6.45	487.61	13.85	3.02%	2.59%	28.56%	No	-	-	-	-	-	-	-	-
650	MI	4.22	4.41	99.53	6.13	0.71%	0.39%	37.65%	No	-	-	-	-	-	-	-	-	-	-	-	-	-	-	-	-
708	DO	5.25	4.87	68.80	5.41	0.65%	20.93%	7.12%	Yes(Mild)	-	-	-	-	-	-	-	-	-	-	-	-	-	-	-	-
798	DO	4.65	4.66	49.98	4.78	0.34%	20.50%	7.50%	Yes(Mild)	4.55	4.82	168.50	7.80	0.72%	12.79%	18.03%	Yes(Mild)	-	-	-	-	-	-	-	-
851	CS	2.58	4.42	62.21	5.05	0.28%	24.08%	1.74%	Yes(Mild)	5.24	4.84	56.50	5.09	0.40%	24.17%	1.88%	No	-	-	-	-	-	-	-	-
901	CS	6.68	4.99	91.13	6.03	0.71%	23.89%	2.66%	Yes(Mild)	7.29	5.15	145.20	7.22	1.00%	21.51%	4.90%	Yes(Mild)	-	-	-	-	-	-	-	-
946	CS	4.30	4.63	22.77	3.75	0.37%	25.98%	3.28%	Yes	2.75	4.72	81.32	5.95	0.82%	22.58%	6.35%	Yes	-	-	-	-	-	-	-	-
992	CS	3.33	4.52	43.38	4.35	0.37%	25.56%	2.62%	Yes	2.78	4.34	8.63	3.08	0.33%	21.59%	7.56%	Yes	-	-	-	-	-	-	-	-
1050	CS	3.91	4.66	28.65	4.12	0.44%	23.67%	12.38%	Yes	4.89	4.98	152.23	6.88	1.05%	27.66%	6.72%	Yes(Mild)	-	-	-	-	-	-	-	-
1205	CS	5.23	5.02	4.47	3.04	0.45%	35.10%	6.38%	Yes	5.72	5.22	2.24	2.97	0.22%	43.02%	2.07%	Yes	-	-	-	-	-	-	-	-